Purdue University ME 463

Talus Low-G Anchoring System

Final Design Review

Aaron Anderson
Matt Stofleth
Jeff Lutz
Mike Niksa
Harsh Patel

5/02/2016

Executive Summary

This report covers the design and testing of the first Talus Low-G Anchoring System prototype. Past work on defining the problem and project requirements is reviewed, followed by an overview of the concept design process and design solution. After that, the testing and verification process is described along with the testing results and conclusions.

The purpose of the Talus Low-G Anchoring System is to anchor a landing spacecraft onto the surface of a comet in a microgravity environment. The anchor is necessary due to the weak gravity on small astronomical bodies. There are few solutions to the problem of holding a spacecraft onto the surface of a low-g astronomical body, however the European Space Agency (ESA) Philae landing spacecraft was identified to have an anchoring system that serves as a sufficient benchmark for the design of the Talus Low-G Anchoring System. Potential primary customers for the anchoring system include government aerospace organizations (NASA, ESA, etc.) and private asteroid mining companies (Planetary Resources, Deep Space Industries, etc.). The most important or primary requirements from these customers are overall effectiveness of the anchoring system (e.g. how much reaction force does the anchor withstand), and its versatility in regards to potential surface environments that the system is able to operate in. In accordance with these requirements, performance targets were set for the Talus Low-G Anchoring System to achieve.

The conceptual design for the Talus Low-G Anchoring System prototype consists of a percussive digging subsystem, a damping subsystem, a root casing subsystem, and a root subsystem. The device employs percussive motion and expanding surface area techniques in order to maximize performance with respect to providing an anchoring force. Upon contact with the comet's surface, the percussive digging subsystem works to impact the comet surface and break up compacted regolith. It also serves to excite the regolith into motion and thus eliminate any static friction resistance forces. In order to protect the landing spacecraft's main body, a damping system utilizing honeycombed composite material absorbs and smooths out the landing shock from initial contact with the surface. After coming to rest with the main barb tip of the device beneath the surface of the comet, the percussive oscillations stop and the root system deploys. This expands the anchor system's effective grip onto the comet and maximizes the pullout force required to remove it from the comet surface.

The prototype's performance was validated with several experiments using a swing test and a pullout test. The swing test determined the penetration depth of the anchor to judge the effectiveness of the percussive digging system and the damping subsystem. The pullout test determined the overall effectiveness of the root system and compliant flaps by allowing for the force necessary to pull the system out of a medium that simulates the properties of a comet surface to be measured.

Test results indicate that the prototype performs better than the benchmark system for anchoring force (154 N), worse for size and mass (8 kg per anchor), and equal for all other primary requirements. The effectiveness of the roots and percussive digging subsystems requires additional investigation, however they are still promising if certain adjustments are made to the design of the prototype for future analysis.

Table of Contents

1.0 Problem Definition

The problem statement, technical challenges, customers, benchmark, and system requirements are defined and outlined in this section. Work here served as a basis for the project and defined the need for a system to anchor a spacecraft onto the surface of a low-g astronomical body.

1.1 Problem Statement

Space missions to the microgravity environment of a comet or asteroid are a relatively new desire from private companies and space agencies. The only mission attempting to land a probe on a comet or asteroid so far has been the European Space Agency's Rosetta mission with its Philae lander. The mission resulted in a failure of the lander's anchoring system [1]. In addition, there are few other developed concepts exploring a method of anchoring a spacecraft to an asteroid or comet. Team Talus investigated a solution to the problem of anchoring a spacecraft in a low-g environment and produced a prototype demonstrating the ability to provide an anchoring force between a lander and a simulated asteroid or comet surface.

1.2 Physics of Problem

There are various physical problems that need to be considered for designing the anchoring system. First is the total weight of the final design. The final total weight of the anchoring system is vital because many other aspects of a space mission are affected by weight. For example, it takes more fuel to get more mass into space. This makes the payload weight a key component when designing the rocket to get the lander into space.

Outer space is a very hostile environment because of the pressure and varying temperatures. Space is essentially considered a vacuum because it has zero pressure. There are two types of heat transfer that are relevant to this application: conduction and radiation. A significant source of incoming radiation comes from sunlight. For example, being in sunlight for an extended period of time in space can cause a bare metal plate to get as hot as 260 degrees Celsius. Vice versa, being in a shadow for a long period time, such as on the shadowed side of an asteroid or comet, can cause temperatures as low as -100 degrees Celsius [10]. The anchoring system needs to hold its material integrity while in zero pressure and a wide range of temperatures.

The ESA's Rosetta mission took ten years to reach its destination. Any active system would need to work properly after long periods of stagnation. For example, after ten years, a loaded spring may not have the same strength as it did at the beginning of the mission.

Vibrations will also need to be accounted for. When a rocket is used to send a payload to space, it produces vibrations. These vibrations can affect the integrity of fasteners, electronics, and other components for the anchoring system.

There forces experienced by the lander when anchoring to the comet will also need to be understood. The lander will be descending onto the comet at some speed. The Rosetta mission's Philae lander was moving at one meter per second when it made initial contact with the comet it landed on.

Next, a force will be required to stop the momentum of the lander on the surface of the comet. After this, there will be some rebound as the lander tries to bounce off from the surface. This will also require a force to keep it in contact with the asteroid.

The comet's material will also play a part in the forces acting on the lander. For example, the interacting force will vary significantly between a hard surface versus a dusty surface. This is why an accurate material must be chosen and modeled analytically to represent the comet material.

At this stage, the project focused on the mechanical systems for the anchoring device. This means that emphasis was placed on mechanical issues relating to the anchoring system and its mechanisms as well as to the properties of the comet material. A foam material was chosen that has similar properties to that of comet regolith. The other physical problems previously mentioned were not investigated at this stage due to the scope of the first prototype. The purpose of the initial prototype design is to investigate the effectiveness of the anchoring mechanisms. Further iterations of the anchoring system prototype will be needed to address the other technical challenges.

1.3 Customers

There are several potential customers for the anchoring system, and additional indirect customers may be impacted by the success of the design. Each customer, whether primary or indirect, has a unique set of requirements. First considering direct customers, assembly workers have requirements for safety and complexity of the design as well as size, mass, and compatibility with other space systems. The contractors manufacturing the anchoring system will have many other requirements. The most significant requirements for these companies are the overall effectiveness, cost, safety, compatibility, and versatility.

Another group of direct customers are private mining companies. Currently there are two main companies making a push to begin mining asteroids. These companies are Deep Space Industries and Planetary Resources. The short term goal of these companies is to mine water from comets or asteroids that can be processed into fuel [2]. Once refueling stations have been established, mining for rare elements will follow. With these objectives, space mining companies will have requirements regarding the system effectiveness, cost, versatility, and reusability.

The final set of direct customers are government space agencies such as NASA and the European Space Agency. These agencies will have a stake in the success of the anchoring system due to the fact that the mining materials from asteroids provides a great opportunity to gain knowledge about the origins of the solar system. This opportunity exists because asteroids and comets are generally small fragments of the cores of what were once much larger bodies that have broken apart [3]. There is much information to be gained by obtaining materials from asteroids and studying them. These agencies have an extensive set of requirements for the anchoring system, the most significant being effectiveness, cost, environmental interference, versatility, and human safety.

Indirect customers such as researchers working through space agencies have requirements for the system's effectiveness, and environmental interference. Material processors and consumers using

products made with the mined materials are concerned primarily with cost. Lastly, government agencies will regulate safety.

1.4 Benchmarks

The benchmark for the Talus Low-G Anchoring System is the harpoon anchor that was used on the Rosetta mission's Philae lander. This mission was organized and conducted by the European Space Agency. This particular anchoring method failed to properly initiate, advocating a necessary redesign of the system to provide a more reliable anchoring system in the future. This benchmark is useful for identifying and comparing characteristics such as mass, durability, and versatility based on surface conditions.

1.5 Engineering Requirements & Performance Targets

Engineering requirement were generated based on the requirements of the customers. The requirements were ranked to determine which were the most important. Table 1.1 shows these selected engineering requirements as well as the units by which each is measured.

Table 1.1: Primary engineering requirements

Primary Engineering Requirments	
Requirement	**Unit of Measurement**
Overall effectiveness	Force to release, N
Versatility	# of operating env.
Reusability	# cycles of reuse
Size	Size box m^3
Mass	Kg
Complexity	# of parts
Human safety	Relative safety, 1-3 scale

Combining the information from the Philae lander benchmark with the primary engineering requirements, performance targets for the Talus prototype to meet were generated. Performance targets were generated by picking target ranges that improve upon the benchmark performance while at the same time concentrating on improving in the areas that matter most to customers. Included in Table 1.2 are the benchmark performance metrics as well as the performance targets for the Talus anchoring prototype to meet based on the primary engineering specifications.

Table 1.2: Primary performance targets

	Complexity	Size	Mass	Reusability	Versatility	Overall effectiveness	Human safety
	# of parts	Size box cm^3	Kg	# cycles of reuse	# of operating env.	Force to release, N	Amount of risk (1 least, 2, 3 most)
Target	20	1000	0.4	100	3	400	1
Lower Limit	100	3000	3	1	1	100	3

2.0 Design Solution

The following sections describe the subsystems that compose the Talus anchoring device in terms of their intended role in the overall system. They provide in depth descriptions of component functionality and design justifications. Particular design decisions made by this team highlight the numerous opportunities for innovation that are available in a market that remains largely untouched.

2.1 Design Overview

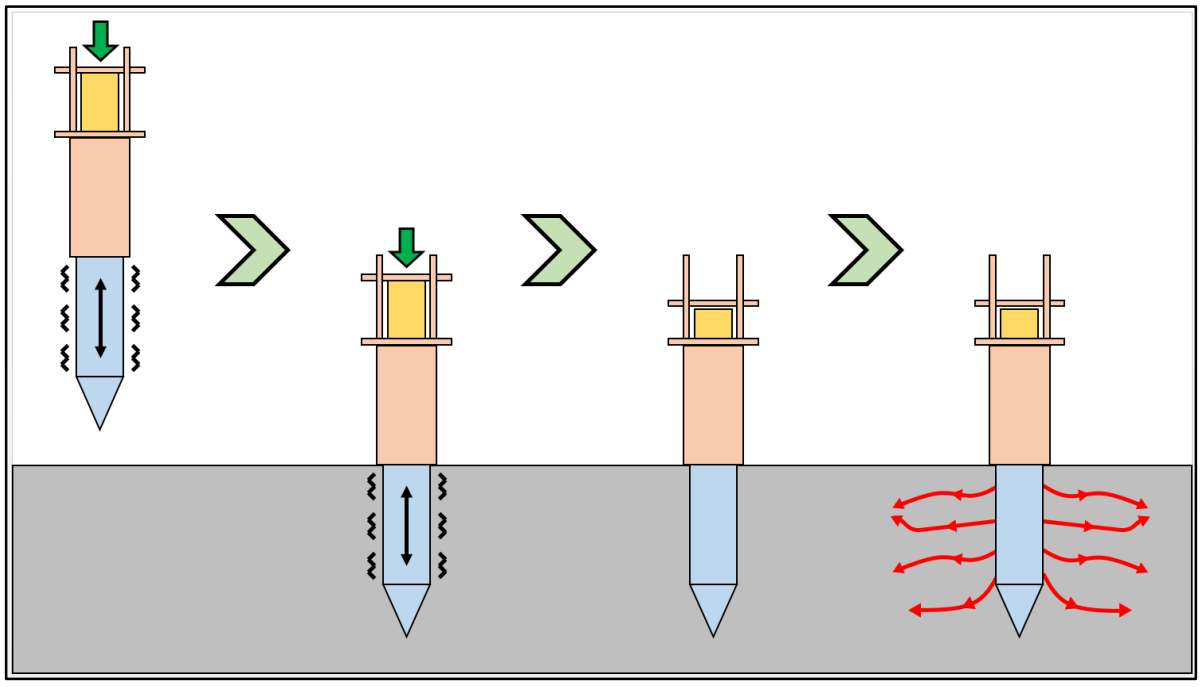

Figure 2.1: A progression of the anchoring system making initial contact with the comet surface. From left to right: 1) The percussive penetration subsystem is engaged upon final approach of the spacecraft. 2) The anchoring system plunges beneath the surface of the comet. 3) The system comes to a rest. 4) The root system deploys.

Figure 2.1 above shows the general design and anchoring process for the anchoring system. The process can be broken up into four stages. Initially, the percussive digging system oscillates the lower barb assembly (colored blue in the above figure) very quickly in a percussive motion. The purpose of the percussive digging system is to allow for a deeper depth to be achieved by the anchor system upon landing. Next, the damping material, colored yellow in the above figure, will begin to compress to help bring the lander to rest. Lastly, roots are actuated out of the root casing. The roots burrow into the surface of the comet similar to how plant roots burrow into soil. These roots increase the effective area of the anchoring system below the comet surface, which consequently increases anchoring force. The lander using this anchoring system would have four legs with this anchoring system attached to each leg, as displayed in Figure 2.2. Figure 2.3 that contains three images of the CAD model of the anchoring system. The fourth image is the built prototype.

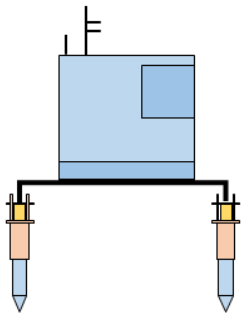

Figure 2.2: A sketch of a hypothetical spacecraft with the Talus Anchoring System attached

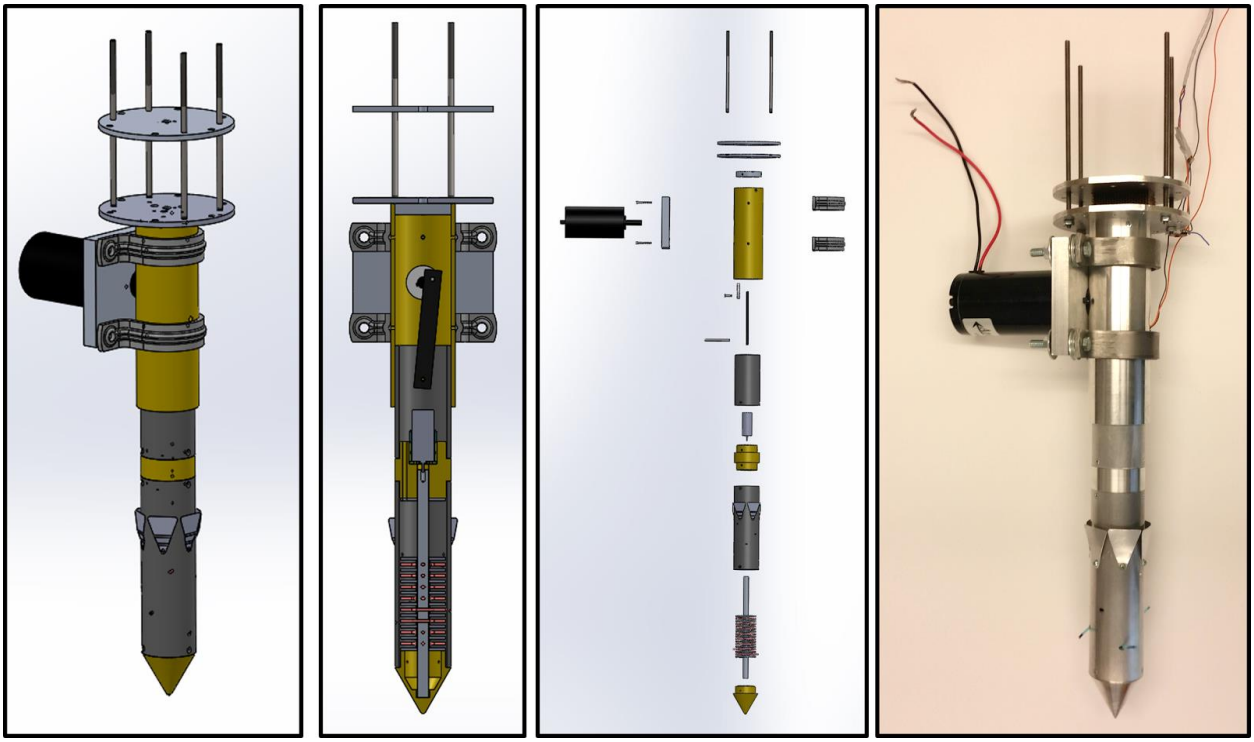

Figure 2.3: Prototype CAD model and built prototype

The Talus Low-G Anchoring System may be broken up into four major subcomponents: impact damping, percussive digging mechanism, compliant flaps, and root system. These four subsystems are a mixture of passive and active components such that catastrophic failure is avoided if any subsystem were to experience loss of power. The dashed lines in Figure 2.4 indicate an internal system and the solid indicate and external system.

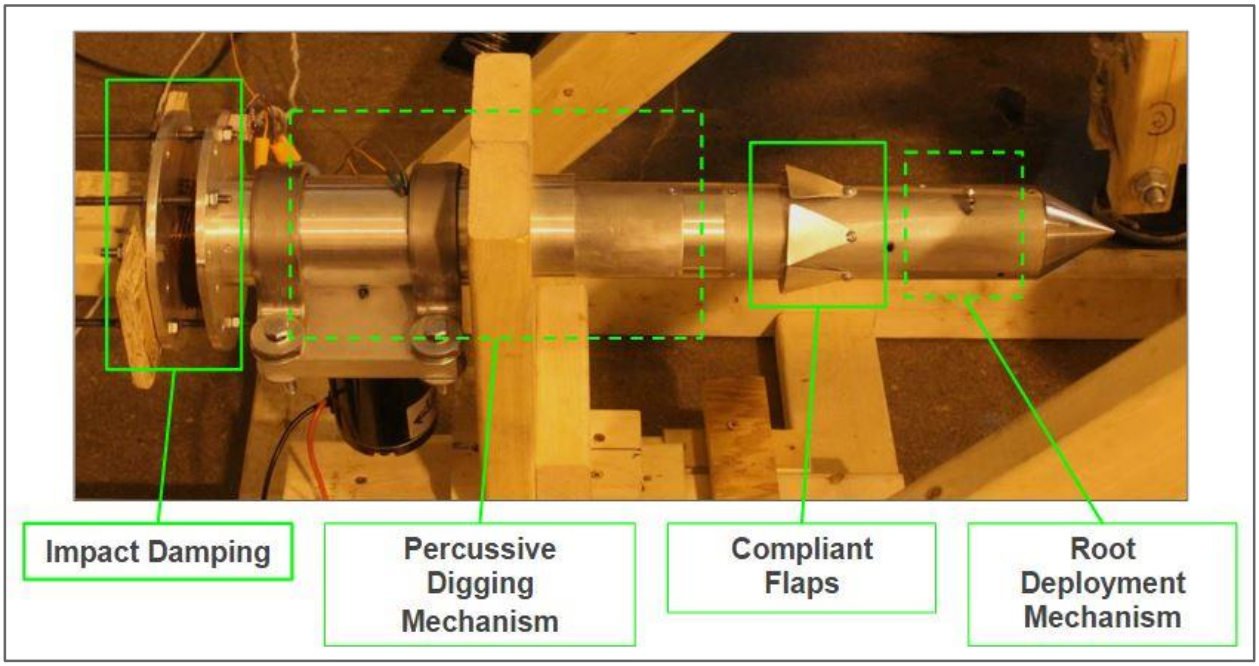

Figure 2.4**:** Subsystem overview

Nomex honeycomb was chosen as the damping material for its availability and similarity to crushable honeycomb aluminum, previously used for lunar landing applications [4]. A crushable substance is a lightweight alternative to a spring and damper system, though it may only be used once. The damping material compresses upon touchdown and greatly reduces the impact force on fragile systems onboard the attached lander. Its measured effectiveness in our testing will be described in later sections.

The purpose of the percussive digging mechanism is to increase penetration depth by loosening surrounding regolith particles and mitigate effects of their cohesive forces. A motor turns a slider crank mechanism within the outer structure tube to oscillate the lower assembly in a percussive motion.

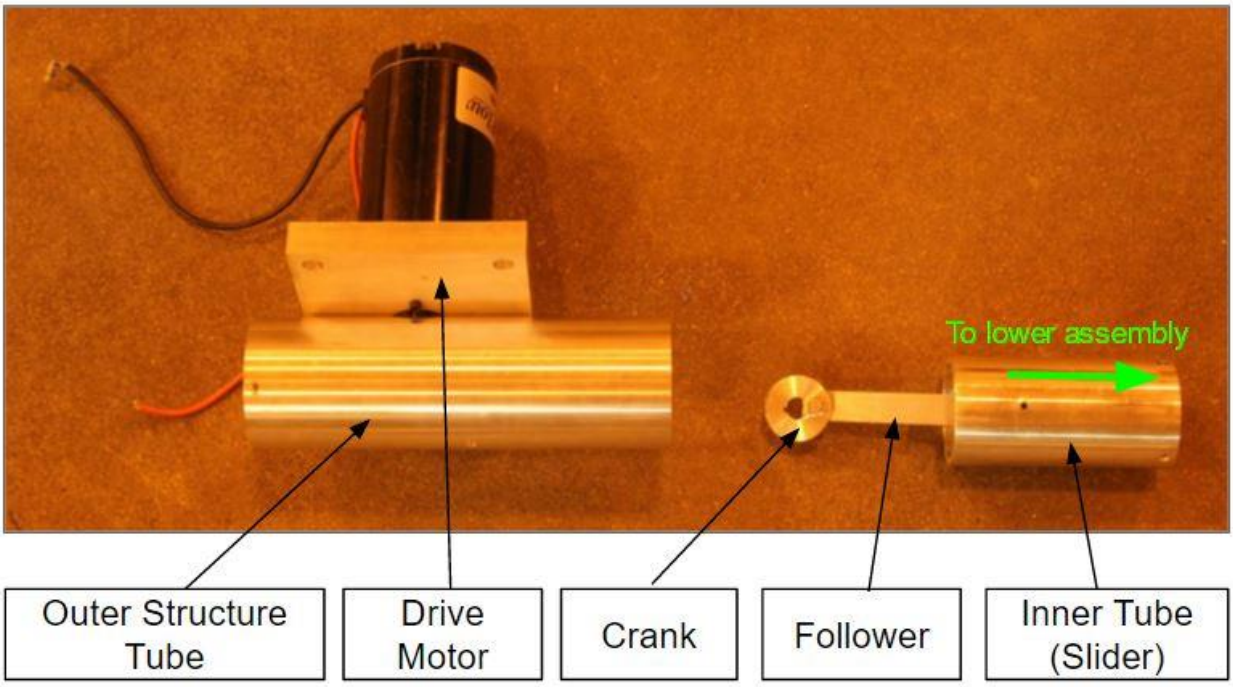

Figure 2.5: Percussive digging mechanism components

Flaps cut from 30 gauge aluminum sheet metal are fastened circumferentially around the casing tube to act as a passive redundancy in the case of root system failure. The flaps are compliant so that after the anchor enters the surface, they bend outward if the system starts to back itself out, creating substantial resistance.

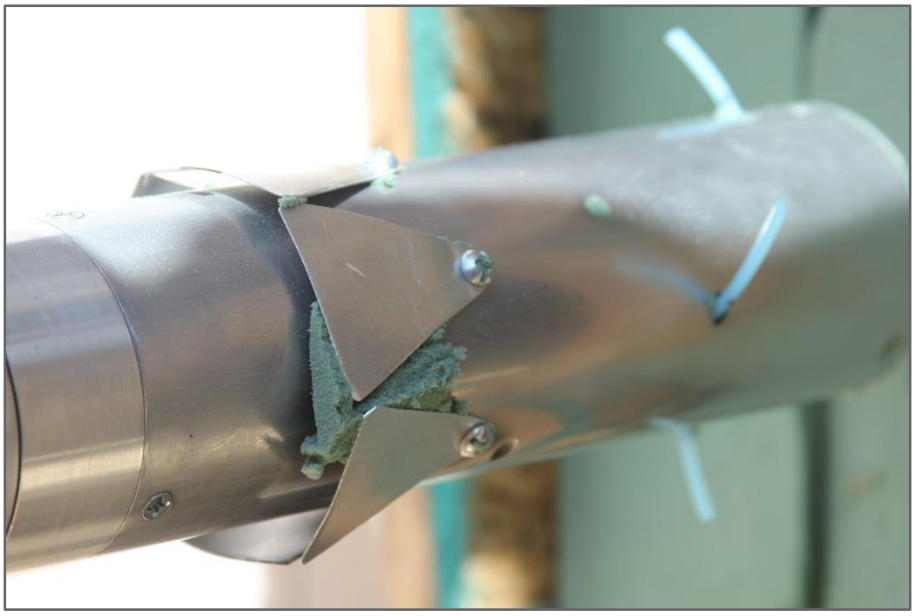

Figure 2.6: Compliant flaps

This prototype features four stiff, plastic cords serving as the “roots” for the primary active anchoring system. The cords attach to an aluminum rod that is rotated by a 12V DC motor. The roots are retracted inside or near the outer surface of the casing tube during initial penetration to reduce drag. Upon deepest penetration, the roots are actuated from the casing to a predetermined effective diameter. The purpose of the root system is to increase the regolith column area above the roots, thus increasing the amount of cohesive forces between the particles. This ultimately increases the amount of force required to pull the anchor from the regolith.

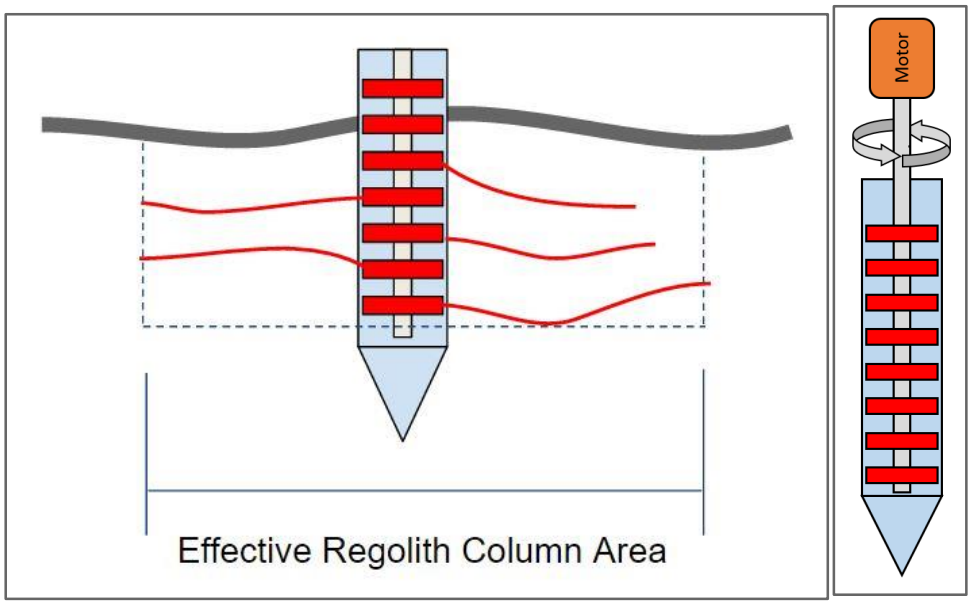

Figure 2.7: Root subsystem

The Talus Low-G anchoring system outperformed its primary benchmark, the Philae harpoon anchoring system, in a few critical areas including overall effectiveness, complexity, and human safety.

Table 2.1**:** Benchmark comparison

Primary Requirement	Unit of Measurement	Talus Anchoring System	Philae Harpoon Anchoring System
Overall effectiveness	Force to release (N)	622.75 (25” drop height)	< 330
Versatility	# of operating env.	2	2
Reusability	# cycles of reuse *per anchor	1	1
Size	Size box (in^3) *per anchor	142.61	84.88
Mass	kg *per anchor	7.94	0.45
Complexity	# of parts *per anchor	20	27 (est.)
Human safety	Relative safety, 1-3 scale	2	3

The team expected to underperform in the mass category due to the limited budget, granting primarily the use of cheap, heavy, and unrealistic materials. The final product might include composite material substitutes in some areas, shedding a hefty amount of undesired weight. The Talus prototype was deemed safer than the Philae alternative due to the lack of compressed gas elements and high-speed projectiles, both present in the benchmark lander's harpoon system.

2.2 Proposed Advantages of Design

The Talus Low-G Anchoring System Prototype is innovative and is advantageous in comparison to similar systems primarily due to the use of passive anchoring mechanisms that provide redundancy for active ones as well as due to its unique mechanisms for holding onto a comet's surface. Existing anchoring devices and concepts such as the European Space Agency's Philae spacecraft do not employ passive anchoring techniques that will work in the event of an active systems failure. The Talus Low-G Anchoring System is innovative in that there are passive flaps on the anchor that are intended to provide anchoring force even if the active root system fails. The design also shows innovation through the use of percussive motion to increase anchor penetration depth. Although it has been incorporated in spacecraft sample collection devices, percussive mechanisms have never been developed or attempted on a spacecraft landing apparatus. Another unique aspect of the prototype is the root subsystem. This one-of-a-kind anchoring concept draws inspiration from the ability of tree roots to remain secure in the ground in a variety of conditions that could otherwise uproot the trees, such as in high winds or for trees growing out of cliff faces. The use of passive and active redundancies coupled with the percussive motion and expanding surface area techniques in the Talus Low-G Anchoring System serve to give the design the potential to be more effective at anchoring than the Philae lander's anchor system.

2.3 Subsystem Designs

The Talus Low-G Anchoring System can be broken down into its most important subsystems, which includes the root casing, root assembly, percussive digging, dampening, and structural subsystems. These main systems are outlined in the following sections.

2.3.1 Root Casing Subsystem

The main objective of the root casing subsystem is to reduce the force required to penetrate the regolith, maximize the penetration depth during lander impact with the comet surface, and to store the root system. The root casing subsystem is made of three components, which include the casing cone, casing tube, and compliant flaps. Each component is made of aluminum 6061 - T6 for ease of manufacturability and for the potential to have consistent thermal expansion coefficients to handle the extreme conditions in space.

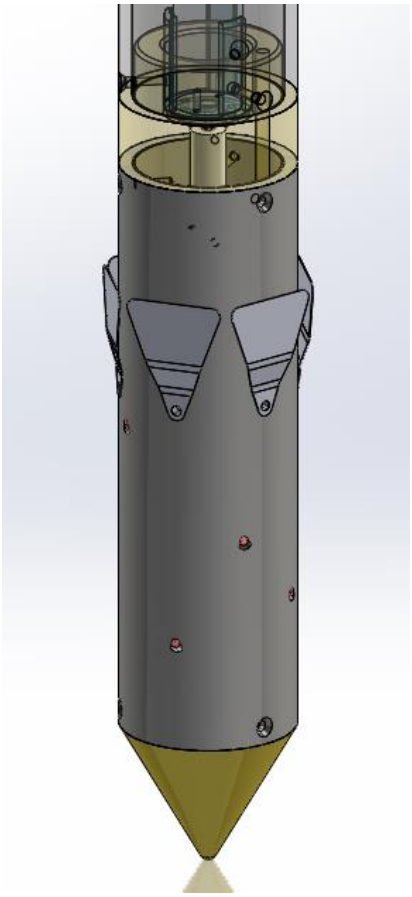

Figure 2.8: Root Casing Subsystem

The casing cone is the first object to make contact with the comet surface. The shape and angle of the casing cone allows for reduced resistance when impacting the comet surface compared to flat, spherical, or ogive anchoring tips [5]. The interior of the cone tip has been machined out to reduce weight, allowing the root rod to sit and rotate freely inside.

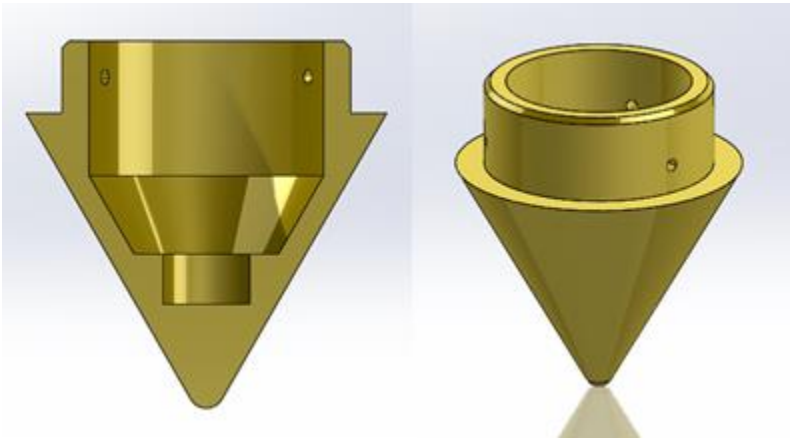

Figure 2.9: Casing Cone Tip

The casing cone connects the cone tip to the structural components of the anchoring system and stores the root assembly system inside. The casing tube consists of eight angled holes to allow the roots to be guided out of the casing during deployment. Above the root casing holes are the compliant flaps.

Figure 2.10: Casing Tube

The compliant flaps complement the root system by adding additional surface area to the anchoring system with the purpose of increasing the pullout force of the device. Six compliant flaps are utilized around the circumference of the casing tube above the root system, as seen in Figure 2.8. The objective is to utilize both active and passive anchoring systems in order to ensure a backup is available in case a subsystem fails to deploy. The compliant flaps are made of sheet metal which is easy to form in order to get the desired shape of the flaps. The flaps are flexible enough to contour towards the casing tube during impact and contour out during pullout to give more anchoring surface area. This allows the flaps to hug the casing tube and negligibly affect the penetration depth of the device during impact. Depending on the compressive strength of the comet surface (7 to 100 kPa), the force required to pull out the flaps will range between 9.28 N (2.09 lbf) and 132 N (29.7 lbf) respectively, assuming the system reaches the desired penetration depth of 0.23 m (9 inches) [5]. Section 7.3 Appendix C goes into further detail about the derivations involved in calculating anchoring force, resistive penetration force, and penetration depth.

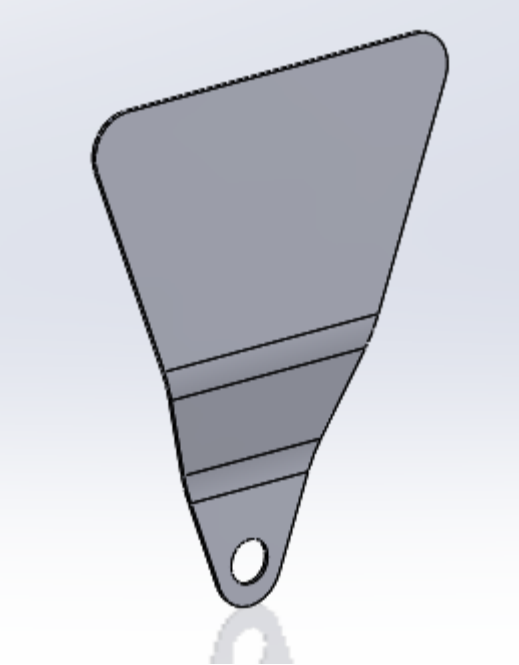

Figure 2.11: Compliant Flaps

2.3.2 Root System

One main issue with anchoring a spacecraft in a low gravity environment is the presence of reaction forces during landing or normal operations that can push the lander away from the comet. The Philae lander was designed to use a small thruster on its top surface that would push the lander into the comet. This was to compensate for any reaction forces that might have pushed it back from the comet's surface during anchoring deployment. Various mechanical systems were investigated to counter reaction forces for the Talus Low-G Anchoring System. The main concept that was considered is a root like anchoring system. A rotational torqueing actuator system was designed for the roots, which can be seen in Figure 2.12.

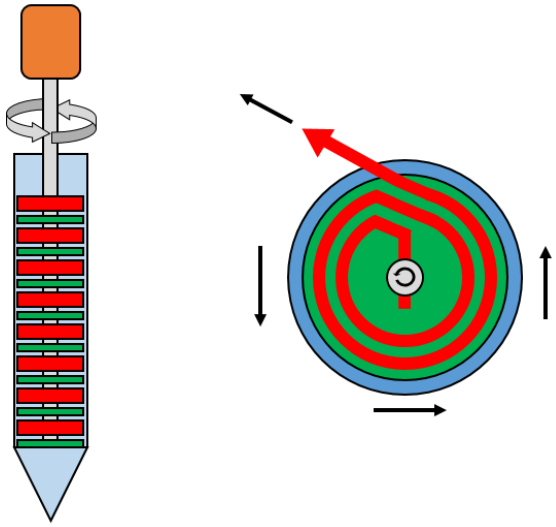

Figure 2.12: Rotational root actuator

In the rotational actuator design shown in Figure 2.12, red indicates the roots, the green is spacers, and the orange is the motor. Each root gets its own plane, and each root is separated by a spacer. The roots are designed to be stiff enough to keep relatively rigid during deployment, but flexible enough to fit into the root casing. The motor applies torque to a shaft that transfers the torque to the base of the roots which pushes them out of the casing. This mode of actuation keeps all the forces planar with the surface of the comet, and prevents the actuation of the roots from pushing the lander away from the comet. The model of the root system can be seen below in Figure 2.13.

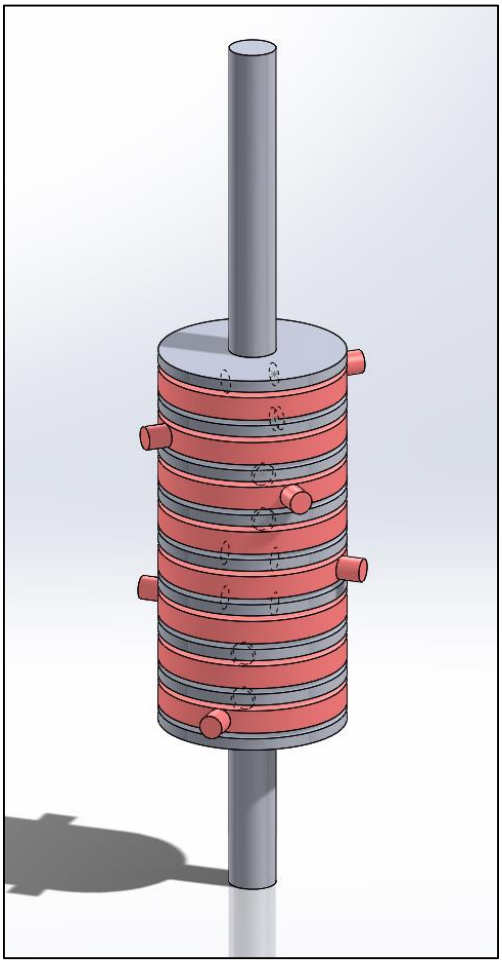

Figure 2.13: Root assembly that will be inside of root casing

The inner diameter of the root casing is 5.08 centimeters. Taking into account this size constraint, there can only be so much length of wire that can fit into the confined space. Calculations, which can be seen in 7.3.4 Appendix C, show that a rough maximum of 25.4 centimeters of wire can be packed into the root casing.

We have used multiple methods to estimate the anchoring force produced by a single root. Estimates are mainly determined by the root geometry and strength of the comet material. The very nature of the chaotic roots flexing through the comet also makes it difficult to calculate an accurate anchoring force. For now, the estimates show an anchoring force range of 1 to 71 Newtons. Further experimentation

with the anchoring system will demonstrate the role that the roots play in the effectiveness of the anchoring system.

The motor that drives these roots needs to provide at least 0.2 N-m of torque. Again, because of the chaotic nature of the roots, testing and experimentation was done to show if a stronger motor than the one chosen will be needed. Initially, a high torque twelve volt motor will be used to actuate the roots. This motor was capable of actuating the roots for the prototype.

2.3.3 Percussive Digging Subsystem

The purpose of the percussive digging subsystem is to reduce the force necessary to plunge the anchor into the surface of the comet. In one experiment performed by Honeybee Robotics, the utilization of percussive techniques reduced the force required to push a shovel into simulated lunar regolith by 15 times [6]. The Talus Low-G Anchoring System employs a percussive mechanism to allow it to penetrate further beneath the surface of the comet. The benefit of deeper penetration is an increased anchoring force provided by the barb assembly.

Similar devices in the past have used a percussive digging apparatus operating at a frequency on the order of 45-85 Hz imparting an impact energy between about 0.5 and 2 joules. Frequency of impact was determined to be unimportant based on information regarding regolith mechanics as discussed by Ettourney et.al. [7], however findings from initial tests with the subsystem suggest otherwise and are discussed in Section 4.3. The stiffness and damping properties of regolith in a microgravity environment are likely so small that any mechanical excitation will allow for a resonance like response from the regolith particles. This implies that any mechanical excitation whatsoever will be sufficient to cause resonance in the regolith layer closest to the anchor mechanism reducing static friction forces and thus allowing it to penetrate the surface in an easier manner.

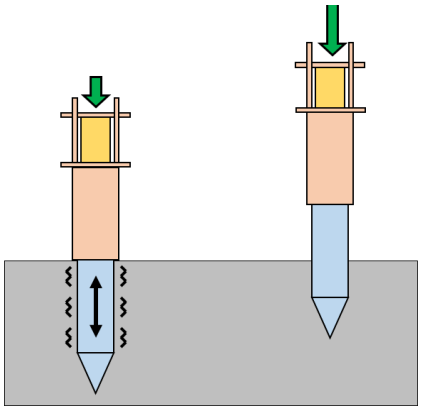

Figure 2.14: Percussive motion in the anchoring device will allow it to travel deeper into the surface of the comet than a similar device that does not use percussive systems.

The parameter of primary importance in regards to percussive digging is impact energy. Impact energy determines if the mechanism will be able to break up tough material that it encounters on the surface of the comet. The target impact energy for the Talus Low-G Anchoring System will be between 2

and 5 joules. Since target impact energy is difficult to determine analytically, the 2-5 joule range was selected based on the experimental results published by Honeybee Robotics [6].

Due to budget, complexity, and time constraints, the slider-crank mechanism was deemed to be most appropriate for the prototype. The slider-crank is able to replicate the motion and impact energies that are of primary concern at a low cost and with a relatively low mechanical complexity. More effective options to replicate this motion in future iterations of the design are discussed in Section 4.3.

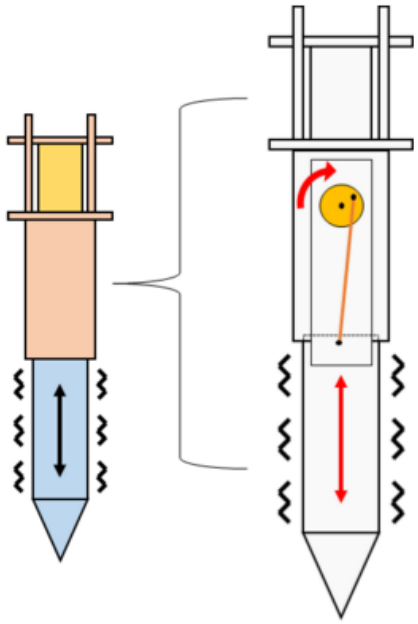

Figure 2.15: Slider crank mechanism that enables percussive motion

A kinematic analysis of the slider-crank mechanism was performed to determine the acceleration of the barb assembly and the rotational speed of the crank link. From there, the required rotational speed of the crank link was determined to be between 1000 and 2000 RPM by using energy analysis and a desired impact energy. The required input torque was calculated to be between 4 and 9 newton meters by analyzing the forces seen at the barb tip and the inertial forces from the slider-crank movement. The motor was selected based on the required speed and torque to drive the slider-crank mechanism as seen in Table 2.2. The selected motor is relatively large, however it was available for immediate use and is suitable to demonstrate the percussive digging technique. Further force analysis was carried out on the links and motor mount fixture to size components and fasteners. Aluminum 6061 T6 with standard steel socket head cap screws are sufficient for the forces involved. Calculations and results of the kinematic and force analyses can be found in 7.3.3 Appendix C.

Table 2.2: Resulting motor sizing parameters

Motor torque, Nm	7.5
Frequency, Hz	25
Impact energy, J	3.5

One of the technical complications involved with the selected motor is the amount of current it will draw. The motor will draw 100-200 amps nominally and 300 amps at stall. This high current will be dealt with using a motor driving circuit with a large relay. A schematic of the motor driver circuit can be found in 7.3.3 Appendix C.

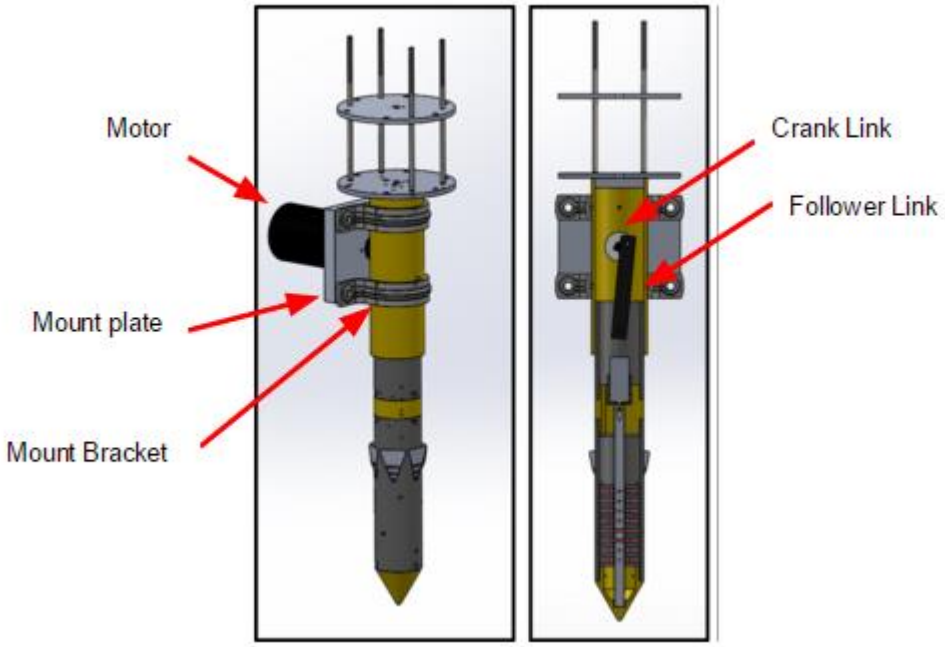

Figure 2.16: Percussive digging subsystem CAD image. The left image shows the drive motor and its mounting bracket. The right image is a section view of the assembly showing the slider crank mechanism.

2.3.4 Damping Subsystem

The damper is an important subsystem for the anchoring system because it absorbs a portion of the excess energy that is not utilized when driving the anchor into the regolith. The lander will be carrying fragile equipment and minimizing the acceleration on these instruments is necessary to protect them. Additionally, the damper isolates the vibration used in the percussive digging system from the rest of the lander body. A piston cylinder fluid damper was not chosen due to the low pressure operating environment of the anchor. Springs were also avoided due to their tendency to create an upward rebound force as the spring decompresses after landing. The damper design is comprised of a top and bottom plate, four threaded rods, and an energy absorbing material between the plates.

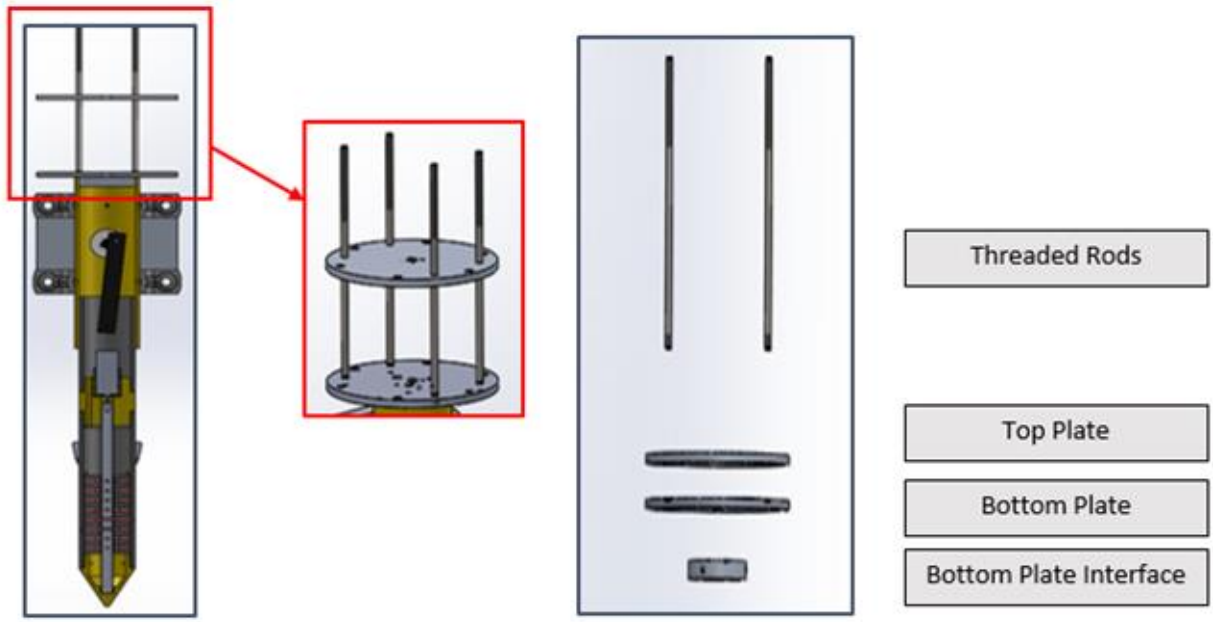

Figure 2.17: Damper components

The bottom plate of the damper is made of .635 centimeters (¼ inch) thick aluminum 6061. To the underside of the bottom plate, a 6.35 centimeters (2.5 inch) diameter rod extending 1.27 centimeters (0.5 inches) is attached. This rod has 3 6-32 tapped holes bored into it to provide a secure interface with the outer tube structure. There are 4 ¼-20 threaded holes through the bottom plate where the four threaded rods are attached. The top plate is made of .635 centimeters (¼ inch) thick aluminum 6061 as well. There are four through holes in this plate to allow it to slide along the rods mounted to bottom plate. There are nuts locked at the end of each rod to hold the top plate in position with the damper material placed between the plates. There are additional .635 centimeters (¼ inch) unthreaded through holes in the top plate that are used to mount the top plate to the test rig with bolts.

The damping material was placed between the top and bottom plate. The damping material selected was .3175 centimeters (⅛ inch) Hexcel Nomex crushable honeycomb, commonly used in racing vehicles and spacecraft. Repeated compression tests on 2.54 x 3.81 centimeters (1 x 1.5 inch) pieces were performed to determine the compressive strength of the material. After averaging the test results it was determined that the material had a compressive strength of 208.4 kPa. Two pieces of honeycomb, each with a compression area of 12.9 square centimeters (two square inches) were placed between the damper plates for each impact test. For an impact velocity of three meters per second, it was calculated, as shown in 7.3.5 Appendix C, that the force over the area of the damping material was high enough during impact to permanently crush the honeycomb. The result is a portion of the excess energy is absorbed and the permanent nature of the deformation minimizes the rebound force that would be created by springs and foam damping materials. The lack of reusability of the Nomex honeycomb was the main drawback as new sections of honeycomb material were used with each test performed, adding cost.

Accelerometers were attached to each damper plate during testing. The accelerometers measured the acceleration of each plate during impact. Max acceleration for each accelerometer was recorded and compared after each test for analysis.

The effect of the damper component of the Talus Low-G Anchor System is critical for analyzing the impact, penetration depth, and pull out force. However, the crushable honeycomb damper simulates the effect of a more complex design that would be utilized in an actual application of the anchor in space. For example, the ESA's Rosetta mission lander Philae had a damping system consisting of motors that converted linear impact motion to heat energy.

2.3.5 Structures

The structure of the anchoring system joins the top and bottom sub-assemblies together and are also used as a component of the percussive digging system. A balance between weight and performance was found in order to accomplish a sturdy skeleton that could support predicted loading while being light enough to not over encumber the anchoring system.

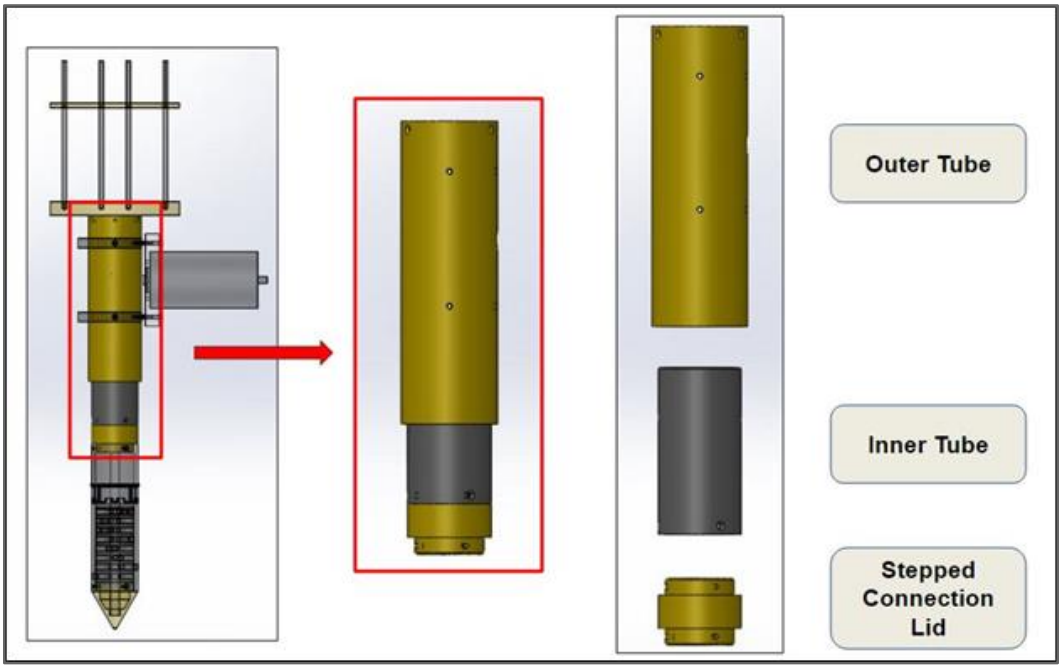

Figure 2.18: Structure component outline

To avoid stress concentrators, cylinders were chosen over square tubing as the base shape for the structural elements. Choosing this shape also maintains consistency with the geometry of the lower barb casing, creating a flush outer surface for the first 13 inches, or 33 cm, of penetration that will promote a smooth entry. To further support this effect, countersunk 6-32 machine screws are used as the primary fastener for all structural components. The percussive digging system employs the inner tube as its slider in the slider crank mechanism and the two systems are connected with a 3/16" slotted spring pin mounted to the inner tube. The outer surface of the inner tube is finely polished to minimize friction as it slides continuously within the outer tube. A stepped connection lid connects the inner tube to the barb casing and also reduces the chance of regolith entering the structure.

6061 T6 aluminum was chosen as the structure material for its lightweight characteristics, simple machinability, and because it has proven performance in numerous structural applications. Consistency in component material establishes a predictable thermal expansion behavior and simplifies manufacturing techniques, cutting down overall machining time.

2.3.6 Control Systems

An overarching system-design platform and a microcontroller were chosen to govern motor performance and to regulate the timing of subsystem activation during anchoring procedures. LabVIEW software coupled with a myRIO microcontroller assumed these roles. Familiarity with LabVIEW's visual programming language was the main influence leading to its selection for this project. The myRIO provides a sufficient amount of analog and digital inputs that are required to govern the two accelerometers and two motors present on the anchoring system.

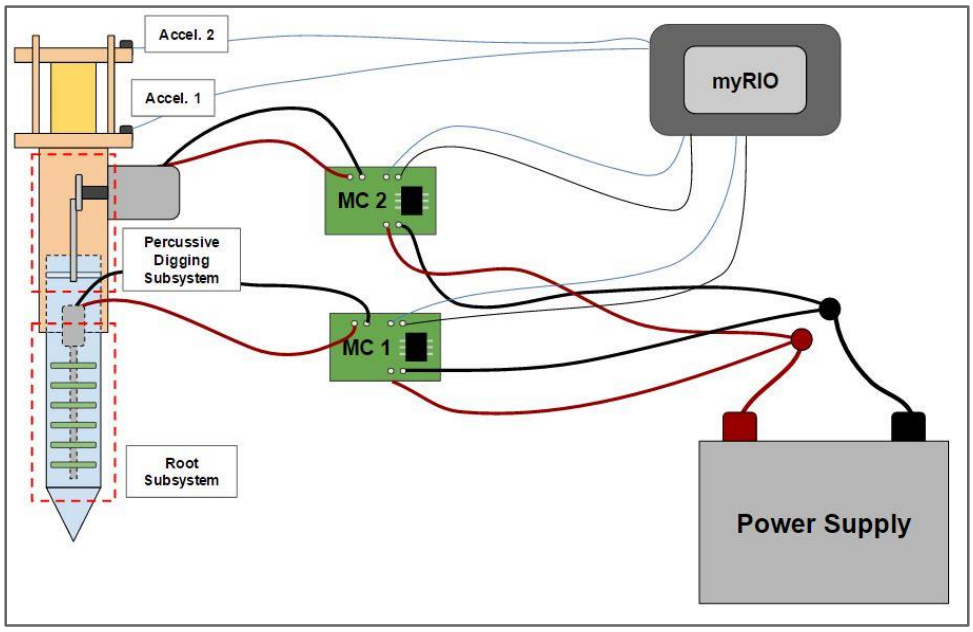

Figure 2.19: Wiring diagram

Two accelerometers mounted directly above and below the onboard damping system serve to track the anchor's acceleration for subsystem activation and deactivation, and also to monitor damping performance. Each motor is coupled with a motor driver circuit for control of the motor's movement. The testing sequence begins with the test rig releasing the regolith box, and the percussive digging system initiated (Step 1). A spike in the acceleration vs. time graph associated with accelerometer 1 indicates that the anchoring system has punctured the comet surface (Step 2). After the anchor has come to rest, the root system is deployed (Step 3). After a certain number of motor shaft rotations has completed to ensure full root deployment the system is shut down, leaving the anchor in a standby position until prompted otherwise by the user.

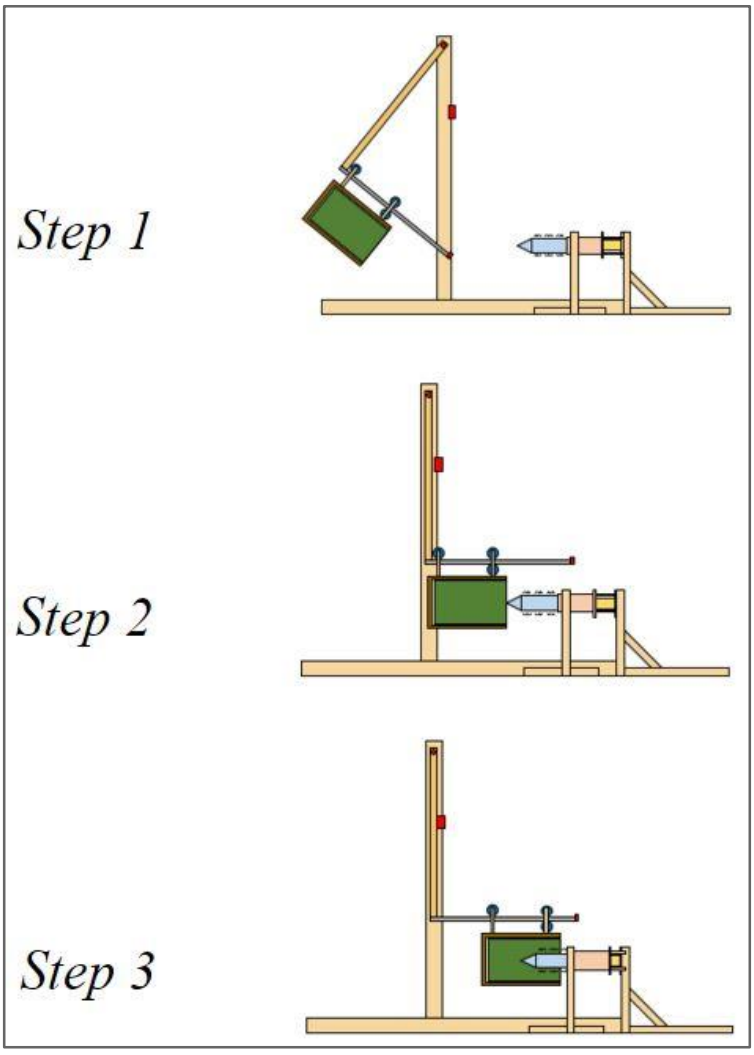

Figure 2.20: Control systems timeline

2.4 Prototype vs. Conceptual Design

There were a few changes that had to be made between the design of the prototype for the Critical Design Report (CDR) and the final prototype that was built. The first difference between these two are the wiring and damper. The wiring was fastened down after the rest of the prototype was put together and therefore was not included in the CDR CAD model. The damper material and size was dependent on test that could only be conducted after most of the prototype was assembled, so it was not modeled into the CAD model. The damping material characteristics were later chosen and implemented into the prototype. The root casing height was increased slightly because of the size of the purchased aluminum cylinder. All other relative dimensions to the root casing height were updated accordingly for the prototype. Also, pipe clamps replaced the mounting brackets that were intended to be used to secure the mounting plate and motor to the outer tube. This was done in order to reduce machining complexity. Additionally, the motor mount plate was extended in width to accommodate the pipe clamps.

The biggest change that was made between the CDR design and the final prototype that was built and tested was the root system. Originally the eight roots were designed to lock and go through the shaft. An issue came up when assembling the root system, such that the roots were getting coiled up improperly inside the root casing. The roots would also get jammed on the way out of the root casing. To eliminate these issues, a more flexible root material with a smaller diameter was used. The roots were fastened to the side of the root shaft for the built prototype. This difference can be seen below in Figure 2.21. This lead to the roots being much shorter for the final prototype at roughly 3.81 centimeters of extension. Also, only four roots were implemented for the final prototype while the CDR had eight roots designed in.

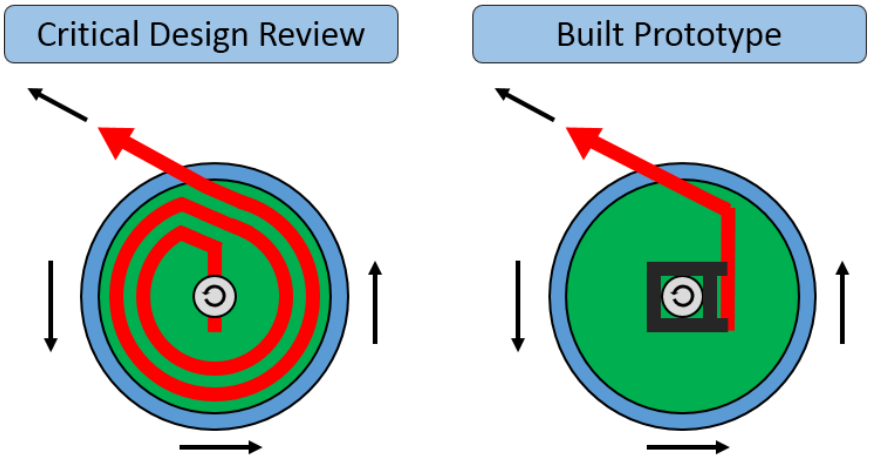

Figure 2.21: Root comparison between CDR and Built Prototype

3.0 Prototype Testing & Validation

Each novel aspect of the Talus Low-G Anchoring System was tested and validated in order to measure its performance relative to the benchmark. The testing and experimentation process for each respective system is discussed in the following sections.

3.1 Testing Materials - Regolith Simulant

A low bulk density, low compressive strength material was desired to mimic the properties of comet regolith. Material strengths of lunar and Martian regolith have been measured numerous times in sample return space missions like Surveyor, Apollo, Viking, and MER rovers. The compressive strength was found to be within the range of 10 to 100 kPa in these missions [8]. This range served as the team's benchmark for selecting our simulant. Phenolic foam, specifically in the form used for floral crafting applications, was selected as the regolith simulant for its seemingly similar mechanical characteristics to the comet regolith.

To ensure that our material selection met our compressive strength requirements, basic compressive strength tests were performed on the material using a hand held force gauge, due to the inaccessibility of more precise measurement machines. Appendix D shows the ten trials performed to determine the compressive strength of the material.

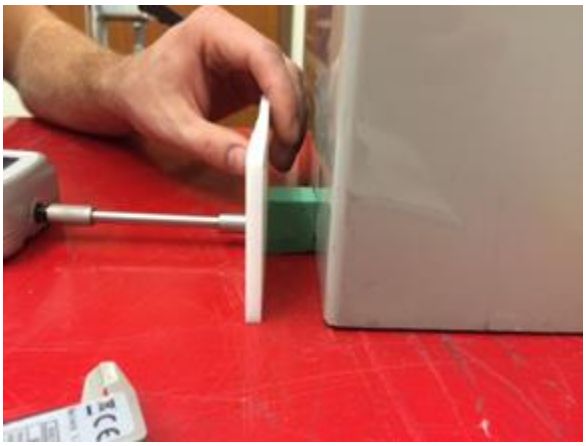

(a)

(b)

Figure 3.1: Compressive strength testing (a) using ~1”x1”x1” phenolic foam samples (b)

An average compressive strength of 62.52 kPa represents the compressive strength of the chosen simulant material, which falls within the 10 to 100 kPa desirable range.

3.2 Experiments

Two main tests were designed to validate the performance of the Talus Low-G Anchoring System so that its performance could be compared to the benchmark anchoring system. The benchmark is the European Space Agency’s Philae Lander from the Rosetta mission. The first test was designed to investigate how deep the anchoring system penetrated into a simulated comet surface upon impact. This test will henceforth be referred to as the Swing Test. The second was designed to test the anchoring force that the prototype provides. The second test will henceforth be referred to as the Pullout Test.

The most important requirement for the anchoring system is that it is effective at anchoring a spacecraft onto the surface of a low-g astronomical body. The performance target for this requirement is that the anchoring system will be able to hold onto the surface while experiencing an upward force above 100 N. The Talus Low-G Anchoring System concept consists of four anchors on four legs of the landing spacecraft. The prototype consists of only one of these anchors, therefore the anchoring force requirement for one anchor is 25 N of force.

The two tests measured the effectiveness of the prototype at providing secure attachment to the surface of a comet regolith simulating medium. Maximizing anchoring force is the primary goal of the prototype and is therefore the primary metric used to measure the effectiveness of the prototype. After the experiments were conducted, the results were compared to the performance metrics from the Philae Lander’s anchoring system as determined by the European Space Agency during testing of the Philae system.

3.2.1 Swing Test Experiment

The depth that the anchoring system is able to penetrate upon contact with the regolith plays a large part in determining the amount of anchoring force that can be sustained before the anchor is pulled out of the medium. This test's aim is to allow for measurement of the penetrating depth of the anchoring system for a landing speed between 1 and 5 m/s.

The prototype was secured to the test rig on the pendulum arm and suspended at a height that allowed for impact to occur between 1 and 5 m/s. This impact speed falls within the desired range necessary to simulate the impact velocity of a spacecraft upon touchdown with a comet. The prototype was turned on just before the regolith simulant was released from its secured height. After impact, the penetration depth of the anchor was marked on the shell of the prototype and measured after the prototype was disengaged from the regolith simulant. The prototype impacted the regolith simulant in the horizontal plane so that the force of gravity had negligible effect on the penetration depth of the prototype.

3.2.2 Pullout Test Experiment

The Pullout Test directly measured the amount of anchoring force sustained by the prototype before it was pulled out of the test medium. The test was conducted immediately after swinging the test medium into the prototype.

After the test medium was swung into the prototype, the root system was either engaged or left alone depending on the experiment that was being conducted. After this, a spring scale was attached to the back of the regolith box. A force was then applied to the spring scale until the prototype disengaged from the surface. At this point, the peak force measured with the scale was recorded. Care was taken to pull straight back on the scale to mitigate unwanted torques and friction from the box's rail system. The scale was also pulled very slowly and at a steady rate to avoid deviations in the measured force from accelerating the mass of the box. The peak force measured from this test indicates the maximum anchoring force that the prototype can withstand.

3.2.3 Experiments Conducted

A variety of experiments were performed using both the Swing Test and Pullout Test procedures in order to validate the performance of the Talus Low-G Anchoring System prototype. The aim of the experiments was to measure the effectiveness of the prototype at providing an anchoring force. This was done by designing a series of experiments to test the root subsystem, percussive digging subsystem, and damping subsystem by varying specific variables relevant to each subsystem.

Initially, three preliminary tests were conducted to ensure all systems were working together properly. The first two preliminary tests were conducted with the percussion turned off, and the last with it turned on.

From there, a series of three tests were conducted. In Table 3.1, these tests are referred to as experiments 4-6. They are combined with experiments 13-15. In these tests, the percussive subsystem was turned off and the roots were not deployed. The penetration depth and pullout force for these tests characterize the prototype's passive performance and the performance of the damping subsystem.

The next series of tests, seen in Table 3.1 as experiments 7-9, were conducted with the same procedure as in the previous tests, except that the roots were deployed after impact with the regolith simulant. These tests were intended to characterize the performance of the root system. Data from the impact of these tests was also able to be used to analyze damper performance since the swing portion of the test was identical to the first round of tests.

After this, the percussive digging subsystem was activated for experiments 10-12 in Table 3.1. These tests were intended to allow for the effectiveness of the percussive subsystem to be analyzed. Due to technical complications, only Experiment 10 was able to be fully completed. Therefore results from this round of testing are speculative at best, however they will still be discussed in following sections of this report.

The final round of testing consisted of varying the height of the regolith simulant box in order to change the velocity on impact, listed under experiments 16-18 in Table 3.1. The prototype was turned off in its passive configuration for these tests. The experiment varied drop height in increments of 15.24 centimeters (6 inches), starting at 91.1 centimeters (36 inches), and ending at 61 centimeters (24 inches) off of the ground. Along with measurement of the penetration depth, the impacts for these tests were recorded. From the recordings, the impact velocity was estimated. These results allowed for correlation of our penetration depth results at any given velocity with a mathematical model produced from a study by Chen and Li [9].

Table 3.1: Table of conducted experiments for performance validation of prototype

Experiment	**Name**	**Notes**
1	Preliminary A	Verifying test rig and prototype operation
2	Preliminary B	Verifying test rig and prototype operation
3	Preliminary C	Static Preliminary A, no roots
4	Damper A	Fix height, x2 blocks, static. couple with test 13
5	Damper B	Fix height, x2 blocks, static, couple with test 14
6	Damper C	Fix height, x2 blocks, static, couple with test 15
7	Roots A	Fix height, x2 blocks, static, root deploy
8	Roots B	Fix height, x2 blocks, static, root deploy
9	Roots C	Fix height, x2 blocks, static, root deploy
10	Percussive A	Fix height, percussion
11*	Percussive B	Fix height, percussion
12*	Percussive C	Fix height, percussion
13	No Root A	Couple with tests 4, no roots, fix height, static
14	No Root B	Couple with tests 5, no roots, fix height, static
15	No Root C	Couple with tests 6, no roots, fix height, static
16	Drop A	Static highest
17	Drop B	Static, medium
18	Drop C	Static, low

* Unusable results or not conducted due to technical complications

3.3 Test Rig

The test rig consists of a wooden frame, which houses the regolith bin and the anchoring system during the tests, as seen in Figure 3.2. The majority of the test rig is made out of 2x4s that provide structural integrity to the rig.

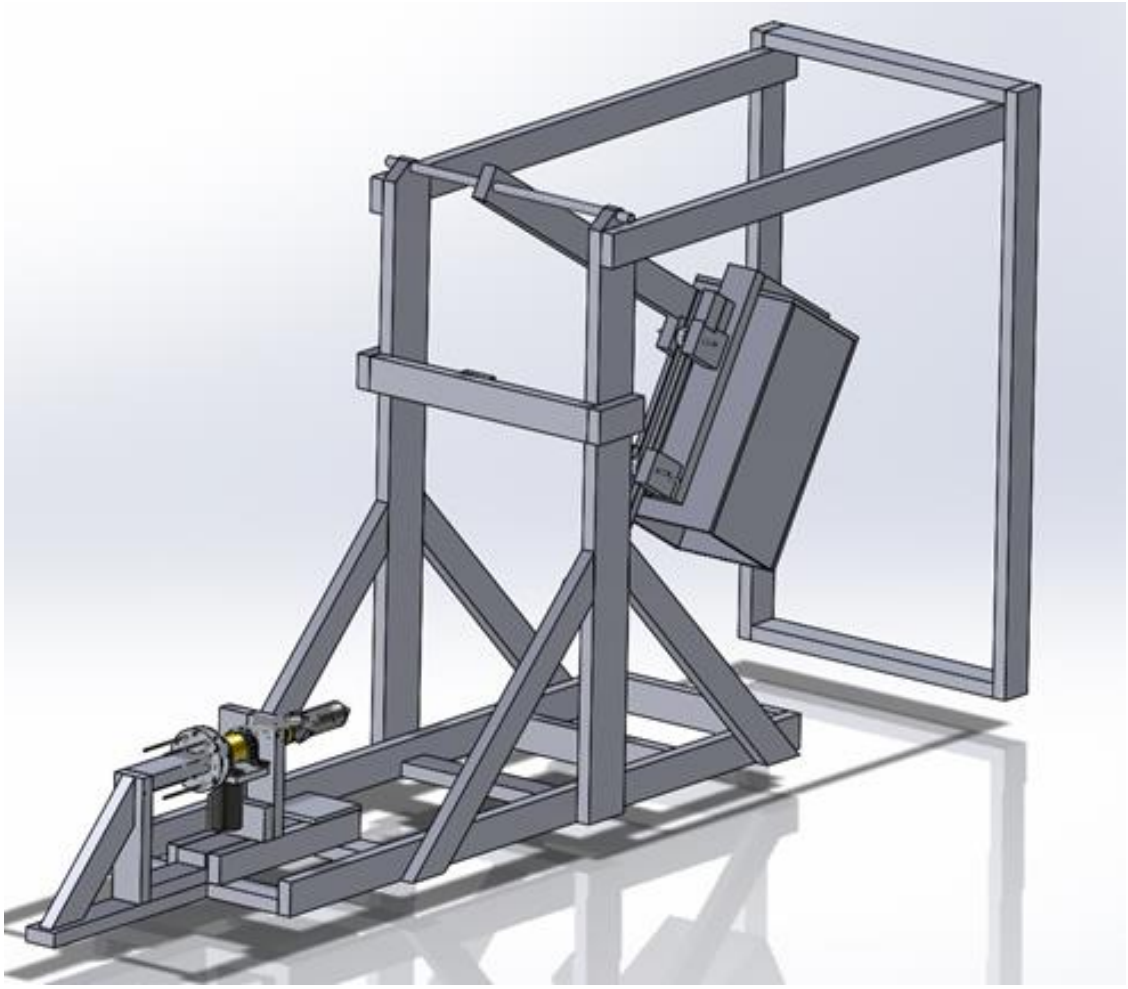

Figure 3.2: Full Assembly Test Rig (Swing Test Configuration)

During the swing test, the wooden frame provides structural stability as it fixes the anchoring system to the base of the rig while the regolith bin and mass is guided towards the anchor. The anchoring slider assembly in Figure 3.3 allows the anchoring system to slide and compress the damper during the impact. The regolith bin in Figure 3.4 houses the regolith simulant foam and is made from wood. On the pendulum arm, a track was constructed in order to convert the rotational motion of the regolith bin into translational motion towards the anchoring unit. The pendulum arm stopper in Figure 3.2 prevents the pendulum arm from overextending, and allows the rail system to be parallel with the floor during swing testing. Penetration depth is recorded by marking the casing tube and measuring the distance from the mark to the cone tip. The expected penetration depth was 12.7 to 25.4 centimeters.

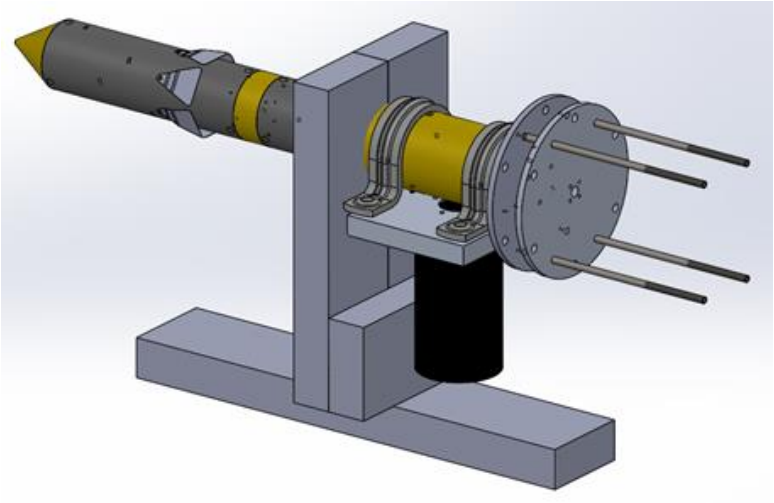

Figure 3.3: Anchoring Slider Assembly

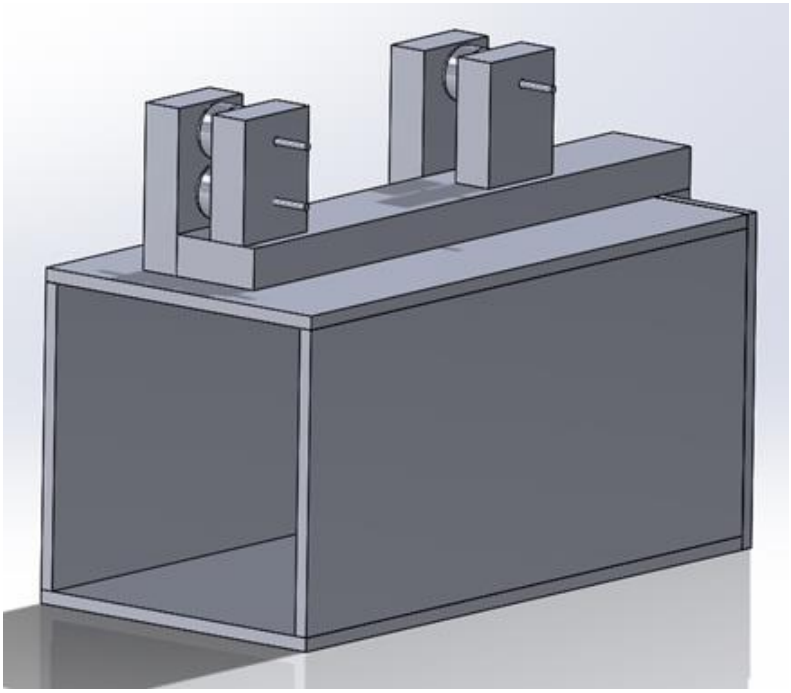

Figure 3.4: Regolith Assembly

The stages of the test rig during testing can be seen in Figure 3.5. In the first stage, the regolith bin is pulled up by a pulley system to a specific height. In the second stage, the regolith bin is released and the pendulum arm locks onto the pendulum arm stopper with a simple latch. In the last stage the regolith bin slides down the rail and makes contact with the anchoring system.

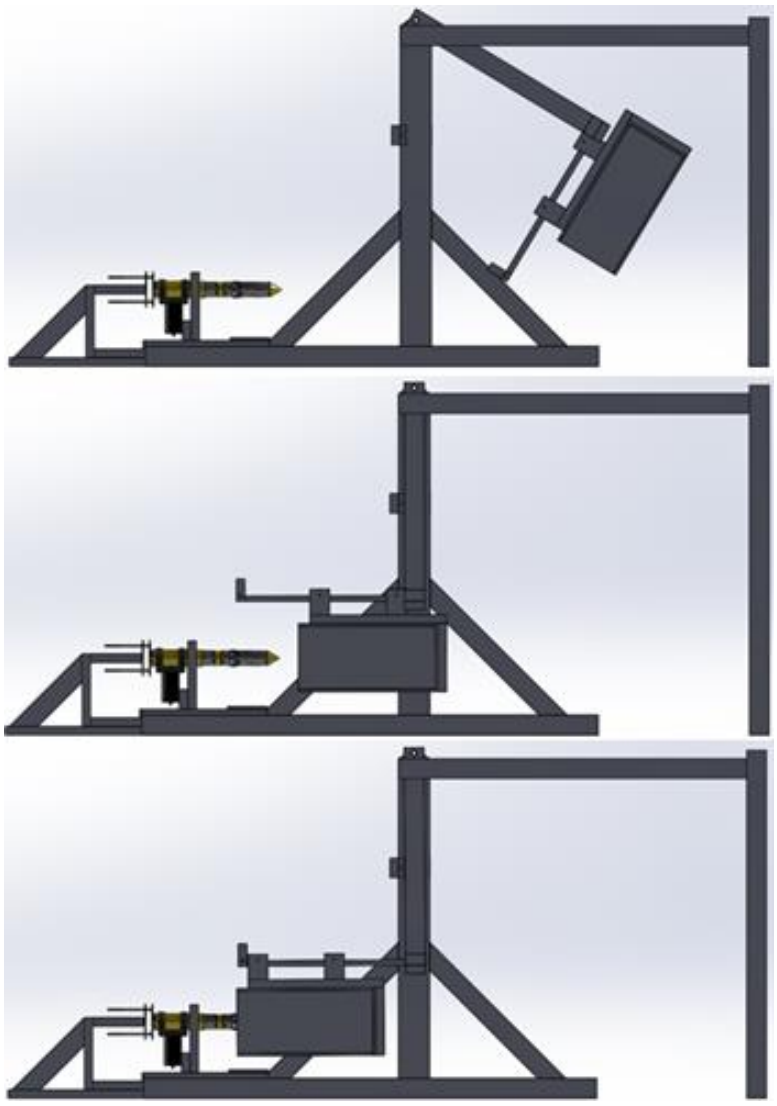

Figure 3.5: Three stages of the Swing Test

For the pull-out test, the pendulum arm is locked into its vertical position to constrain the bin's freedom of movement to only sliding along the rail. The root system was deployed within the regolith bin to simulate full deployment on a cometary body. A handheld, analog force transducer was used to record the force required to pull-out the fully deployed anchoring system from the test bin. The expected pull-out strength of the anchoring system was 25 to 100 Newtons.

There were some specific considerations for how this test rig was designed. A basic pendulum system was chosen because a fairly repeatable impact velocity is obtainable from setting consistent initial height drops for the regolith bin. The anchoring system impacts the regolith parallel to the ground instead of just doing a vertical drop of the anchoring system. This was done so that gravity would not affect the penetration depth of the anchoring system. The regolith bin slides on the rail system which is connected the pendulum arm. This was done so that the anchoring system can continue to penetrate the regolith perpendicularly after it first makes contact.

3.4 Subsystem Validation

Data from all experiments and tests were compiled in a spreadsheet to be analyzed. Data was compiled according to its relevance to any subsystem in question and analyzed to characterize the performance of the respective subsystem.

3.4.1 Root System Validation

Tests 7, 8, and 9 can be compared against tests 13, 14, and 15 in order to analyze the effectiveness of the root system. Each test's data is organized in Table 3.2. All of these tests keep the drop height constant at 106 centimeters. This means all the tests had fairly consistent impact velocities. The consistent impact velocity is also supported by that the consistency of the penetration depths for each test.

Table 3.2: Test data for analyzing effectiveness of root system

Test Number	Roots or No Roots	Drop Height (cm)	Penetration Depth (cm)	Pullout Force (N)
7	No Roots	106.68	24.13	133.45
8	No Roots	106.68	23.50	195.72
9	No Roots	106.68	24.45	164.58
		No Roots Average	24.02	164.58
13	Roots	106.68	24.13	155.69
14	Roots	106.68	23.81	155.69
15	Roots	106.68	23.81	120.10
		Roots Average	23.92	143.83

The data shows the average pullout force actually decreased by roughly 20 Newtons when the roots were deployed. This outcome and its possible causes are discussed in Section 4.1.1. A seen in Figure 3.6 below, the red circle shows where the root was pulled out of the regolith. This means that the roots were able to extend when the anchoring system was embedded into the regolith. It was predicted that pulling the roots through the regolith in this fashion would increase the pullout force.

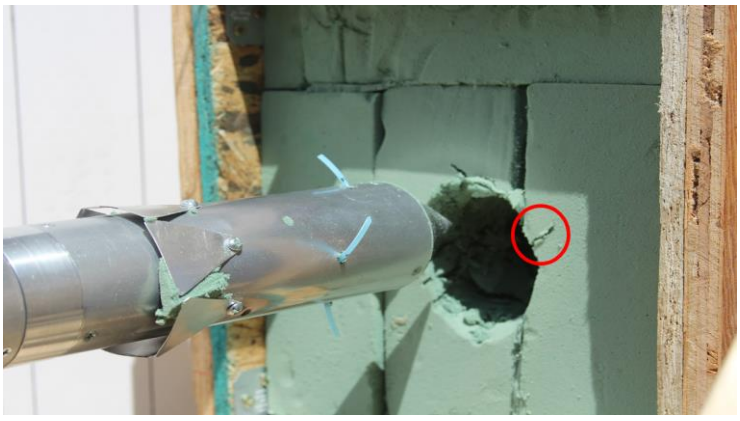

Figure 3.6: Root System Pullout Test

3.4.2 Percussive Digging Subsystem Testing and Validation

The validation of the Percussive Digging Subsystem depends ultimately on how much of an impact the percussive motion has on the depth that the anchor penetrates into the regolith simulant. The purpose of the percussive motion is to increase penetration depth by breaking up the surface material and mitigating frictional cohesive forces from the regolith particles. Therefore it was expected that the penetration depth of the anchor system would be greater with the percussive motion than without it. Data used to judge the performance of the system from testing consisted of penetration depth measurements and video recordings from experiments 5-9, 10, and 15-18 (shown in Table 3.4).

The penetration depth measurements from experiments 5-9 and 15-18 served as baselines for analysis of the Percussive Digging subsystem since the percussive motion was disabled during impact on these tests and all other variables were the same for these tests leading up to impact with the device. Due to technical problems and time constraints, only one useful experiment, Experiment 10, was completed with the percussive motion activated. This severely limits any conclusions drawn from the experimental results, however it does provide some insight for potential future testing and therefore will still be discussed in this section.

For each test used in the analysis for the percussive subsystem, the regolith box was suspended exactly 106.7 cm above the ground. The percussive system, when active, was driven off of a 12 volt, 100 amp hour battery. The voltage was reduced from the original design of 24 volts due to concerns related to the failure of the spring pin on the prototype from a preliminary test with a 24 volt setup and the decision that 12 volts is adequate to drive the percussive motion of the prototype. Upon impact, penetration depth was marked and recorded, and video of impact was taken.

The penetration depth data was averaged across all tests where the percussive system was shut off. This averaged to about 23.97 cm deep which is about 1.25 cm past the compliant flaps on the prototype. The one good test with the percussive motion activated produced a penetration depth of about 18.41 cm. Investigation of the video recording of impact shows that the depth at one point during impact was about 22.9 cm before the box was pushed away by the percussive motion. This intermediate depth is shown in Figure 3.7. The results are displayed in Table 3.3.

Table 3.3: Results of Percussive Digging subsystem tests

Penetration Depth		
No Percussion	23.97 cm	Average
With Percussion	18.41 cm	After bounce
	22.86 + cm	Before bounce

Additional examination of the video results show that there was a significant amount of out-of-plane movement/oscillation from the barb assembly during the percussive motion. This caused a wide hole to form in the test medium at the point of contact with the prototype as seen in Figure 3.8. Additionally, it was noted that upon impact with the test material, the percussive motion seemed to push the box of test medium away from the anchor system

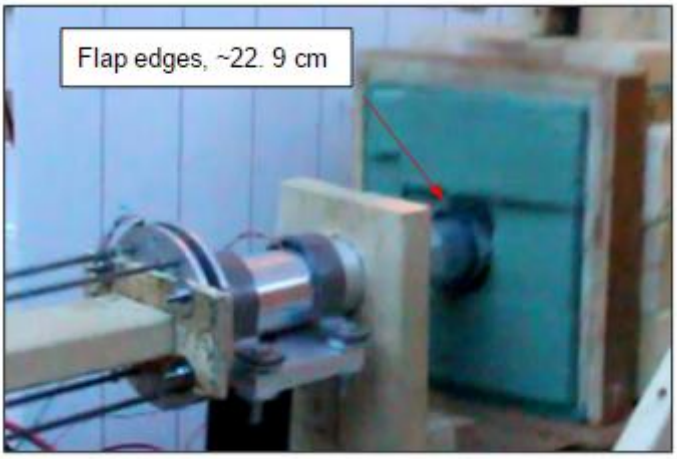

Figure 3.7: Maximum depth achieved during impact before the box is pushed away by the percussive motion.

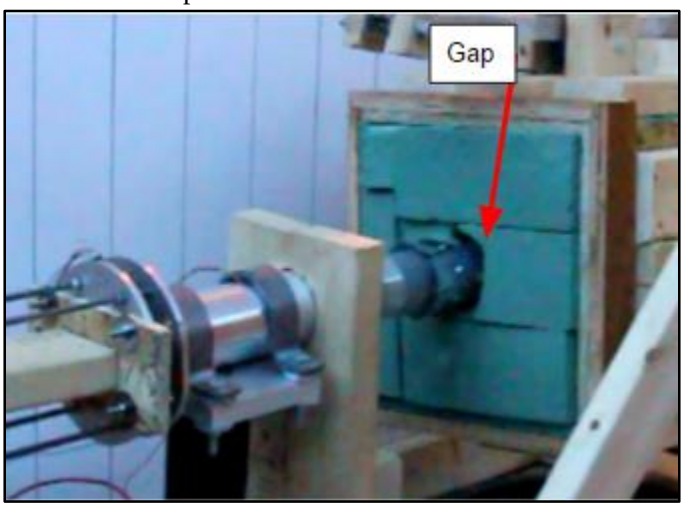

Figure 3.8: Impact of test medium with prototype with percussion activated. Note the wide gap between the prototype and the test medium caused by the out-of-plane motion.

The complication that lead to the inability to perform or obtain useable data from experiments 11 and 12 was due to the sliding mechanism jamming. Upon initial review, it seems that the sliding barb assembly twisted a few degrees off from where it should have been. From there, the slider tube jammed against the outer casing tube.

3.4.3 Damping Subsystem Testing and Validation

To analyze the performance of the damper, three tests were performed. These tests, as labeled in Table 3.1, were tests 4, 5, and 6, and named damper test A, B, and C respectively. For these tests, all test variables were held constant, meaning the drop height was consistent, percussive digging system was off, and identical pieces of honeycomb damping material were used for each test. Accelerometer data was recorded at the top and bottom plate. The bottom plate is the plate mounted to the anchor, and the top plate would be the interface to the actual lander housing equipment. The test data is summarized in Table 3.4.

Table 3.4: Damper Test Data

Test	Accelerometer 1 Max (g)	Accelerometer 2 Max (g)	% difference
4 (Damper A)	1.55657	2.00725	22.453
5 (Damper B)	2.30671	3.37668	31.687
6 (Damper C)	2.1819	2.66392	18.094

In this table, accelerometer 1 was mounted to the top plate or the lander side of the damper while accelerometer 2 was mounted to the bottom plate or anchor side of the damper. Figure 3.9 shows the honeycomb damping material secured between the damper top and bottom plates prior to a test.

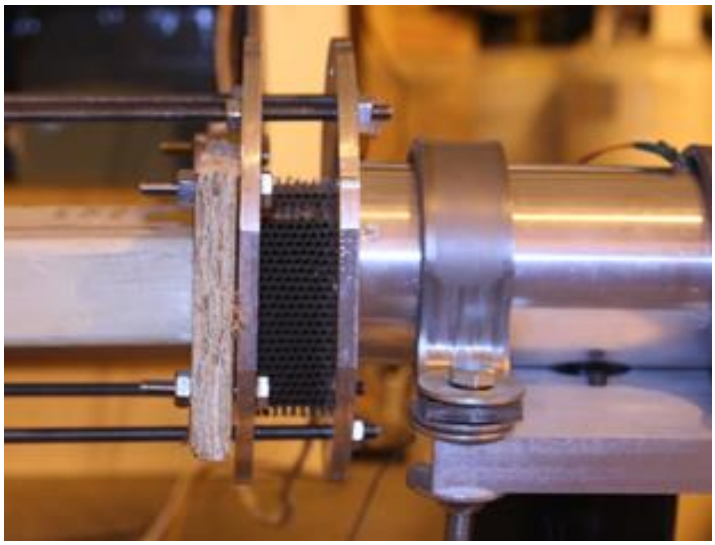

Figure 3.9: Damper Setup

4.0 Testing Conclusions & Recommendations

In this section, results and key findings from each experiment is discussed. Additionally, recommendations for design improvements and the future of the project are made.

4.1 Root System Conclusions & Recommendations

The data presented for the root testing show that the pullout force decreased once the roots were deployed. Figure 3.6 showed the roots were pulled through the regolith, which should increase the pullout force. It is possible this occurred because the passive compliant flaps played a much larger part in the total pullout force, thus overshadowing the effect of the roots. Further testing may be able to reveal the true effectiveness of the roots. There can be some alterations made to the test so as the results can better show the effectiveness of the roots. For example, an alteration can be to remove the flaps, which would leave the roots as the primary anchoring device. This way the friction between the root casing and the regolith simulant material would be the only other source of resistance for pull out force testing.

As previously mentioned, the roots for the prototype did not extend as far as designed within the prototype. These roots will need to go through more iterations of the design process in order to become more effective. Although multiple materials were chosen to be tested for the root material, only one

partially worked. This material was able to extend roughly a 3.81 centimeters out of the casing tube. More extensive testing should be done to find a better suited root material. The key is for the root material to be stiff enough to push through the regolith and flexible enough to fit within the 5.08 centimeter diameter root casing. Once a better material can be found, a longer length of roots can be packed within the root casing, which then in part can allow the roots to extend further into the regolith.

The tips of the roots were cut off to a flat edge for the prototype. Further development on the on an end cap to put onto the root tip may be able to increase the effectiveness of the root system. These end caps on the root tips could be barbed or conical shaped. Essentially, these end caps would decrease the force to push the root through the regolith. They will also increase the pullout force by acting similar to a barb system as in that the end cap digs into the surround regolith when it is pulled on.

Another recommendation to further develop this root system would be to design a more robust connection between the roots and the root torqueing shaft. It was found that attaching the roots to the outer circumference of the shaft was more beneficial for root deployment than securing them through the drilled holes. The root deployment could be even more effective if a specific fastener is used to secure the root to the outside of the shaft.

4.1.1 Potential for Root System Modularity

In future design iterations of the root system, modularity would be an interesting aspect to consider. Currently, the root system consists of a single material and assembly conditioned for a specific type of surface composition, under the assumption that the anchor will penetrate to the proper depth. However, as asteroid and comet landings become more commonplace and surface compositions more defined, it is very likely that utilizing only one type of root design will not be the most effective method of surface adhesion.

The use of interchangeable root “packs” is one interesting method of modulating this root system. Certain packs may be suitable for a tough and rocky subsurface, while others for a powdery surface layer or compositions in between. With a detailed understanding of the landing site’s surface composition, the system could be optimized. Certain packs would be swapped out and set at different depths within the anchor casing based on what’s expected on the surface.

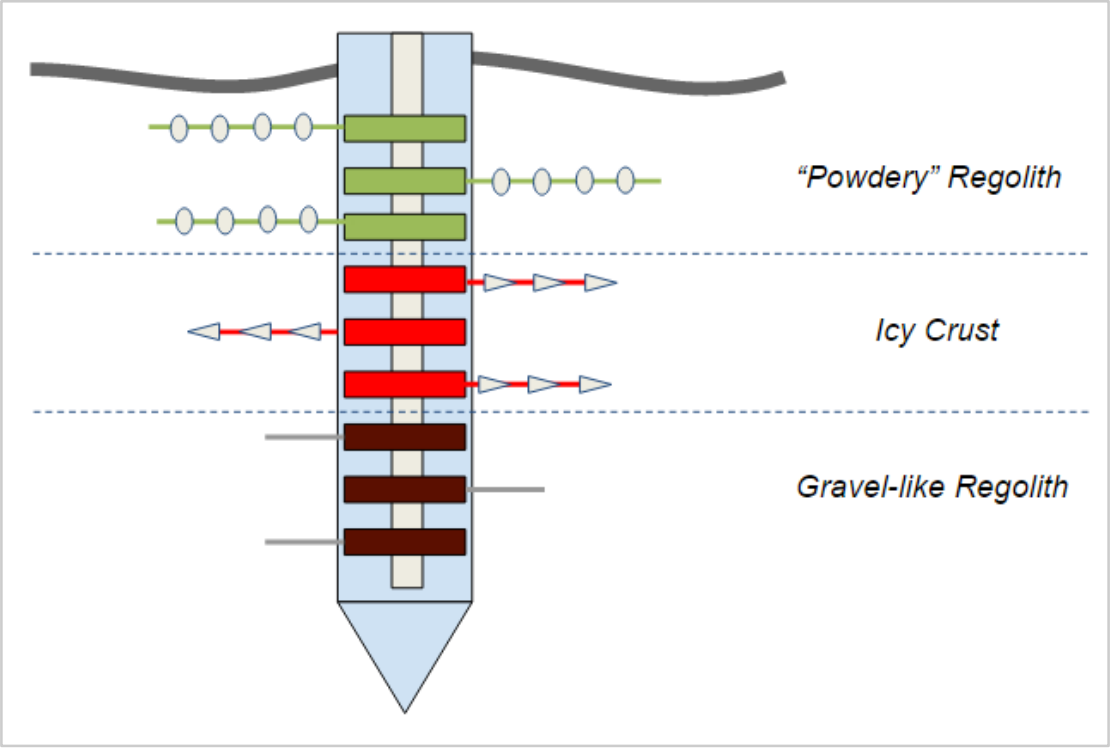

Figure 4.1: Root system modularity

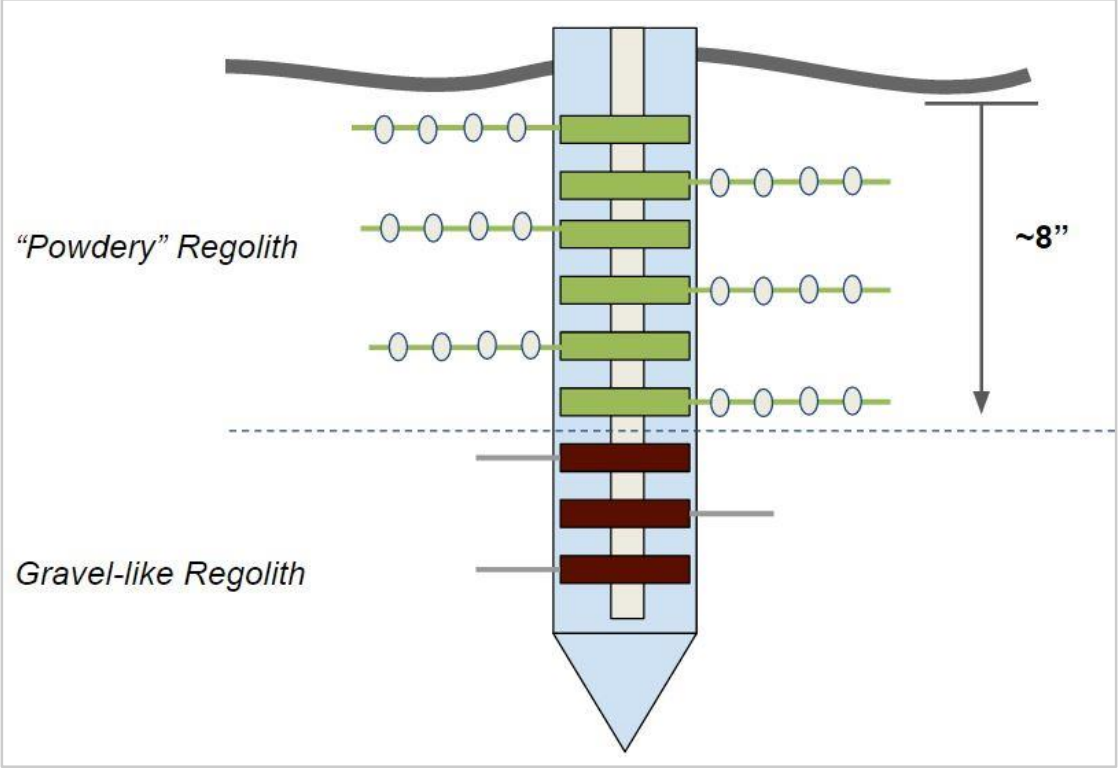

Figure 4.2: Example root packaging for powder dominated surface

For tough, gravel-like subsurfaces a stiff and thin root may be necessary to seek out cracks and develop through them. A similar root design may be used for any icy crust layers, with the added feature of sharp barbs or spikes along the root length. Powdery surfaces could call for attachments that increase surface area concentric with the root diameter with a behavior similar to shovels as the anchoring system attempts to pull itself out.

4.2 Percussive Digging Conclusions & Recommendations

The results of testing and analysis from Section 3.4.3 do not indicate any improvement of penetration of the anchoring system while the percussive motion is active. In fact, in the test case where the motion is activated, the penetration depth after the system came to rest was over 5 cm short of the non-percussive average penetration depth. This result, as mentioned before, is only suggestive of the performance of the percussive digging subsystem since only one useable round of testing was completed with the Percussive Subsystem active. Even though conclusive results cannot be drawn at this point, the available data does provide valuable insight for future testing and improvement of the concept of percussive motion in the anchoring system.

The shallow penetration depth of 18.41 cm seen in the test with the percussive motion active upon impact does not hold up with the prediction that the motion would help increase penetration depth. However, after investigating video recordings of the same test, it is apparent that there are few potential reasons for the small penetration depth seen in the test result.

The video, as mentioned in Section 3.4.3, showed a large amount of out-of-plane vibration of the barb tip assembly during percussion. This unintended movement resulted in unwanted energy transfer to the test medium in the vertical and lateral directions rather than the intended axial direction. Since this energy was not transmitted axially, the penetration depth of the anchor was less than if all of that energy were concentrated in an axial motion. Additionally, the out-of plane motion potentially knocked the test medium's box to the side so that it had the opportunity to interact in unplanned ways with its rail system, resulting in further energy losses due to friction and impacts on the rail. These combined consequences of the vertical and lateral movement of the anchor system during percussion are the likely causes of the shallow penetration depth obtained from Experiment 10.

Additionally, it was noted in the test video that the penetration reached about 22.9 cm at one point during impact as seen in Figure 3.7. The test medium was then observed to be pushed away from the anchor system before coming to a rest at 18.41 cm of penetration depth. The video results seem to show that the percussive motion of the prototype pushes the test medium and its box away for every stroke of percussive movement. Even at its peak depth during impact, the approximate 22.9 cm of penetration depth seen in the video is still almost a half inch short of the average penetration depth from the non-percussive impact test cases.

A likely explanation for this is a combination of consequences from out-of-plane movement and the frequency of oscillation. Upon initial impact, energy is lost from the side-to-side motion of the barb assembly. This loss of impact energy would explain the relatively small 22.9 cm penetration depth during impact. The pushing of the box away from the anchor during the process of impact can then be explained by the cyclical motion of the barb assembly in the axial direction, which is slow enough and has a long

enough stroke to push the test medium and its box away from the prototype until it comes to a rest at 18.41 cm.

It could be that since the system was operating at 12 volts instead of the intended 24 volts (for reasons as described in section 3.4.1), the frequency of oscillation was too low to overcome effects of friction while impacting the test medium.

In moving forward with the analysis and design of a percussive digging aspect for the Talus Low-G Anchoring System, it will be important to consider the results and findings from this initial test. The most important considerations in regards to the theory of percussive digging are to decrease out-of-plane movement of the barb tip assembly during percussion and to increase frequency of oscillation. In regards to mechanical issues, it will be important to address the problem of uniform contact for the sliding surfaces, cyclical fatigue and failure of the spring pin at the bottom of the follower link, and maintaining only axial motion of the barb tip assembly.

One potential solution to decrease out of plane movement of the barb tip would be to add two or more slots for the sliding surfaces to slide along during percussive movement. This would help prevent the smaller tube from bouncing within the confines of the larger tube. Also, tighter tolerances between the two sliding surfaces would eliminate open spaces that allow for large displacements to occur. Finally, increased lubrication of the sliding surfaces would help enable smooth and consistent motion during percussion.

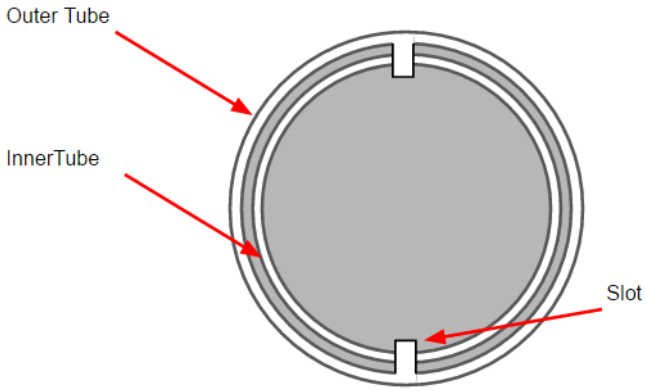

Figure 4.3: Cross section view of slotted system for sliding surfaces.

In order to increase frequency of oscillation, the crank link length could be reduced and the speed of the motor increased by running it at 24 volts or choosing a faster motor. The frequency could also be increased by replacing the motor and crank system with a different means of actuation. One attractive option is a piezoelectric stack actuator. This device is ideal since it is used in aerospace applications, has no mechanical moving parts, and allows for very high frequencies of oscillation at small stroke lengths. A device such as this would eliminate most of the problems stemming from impact with the test medium as discussed previously.

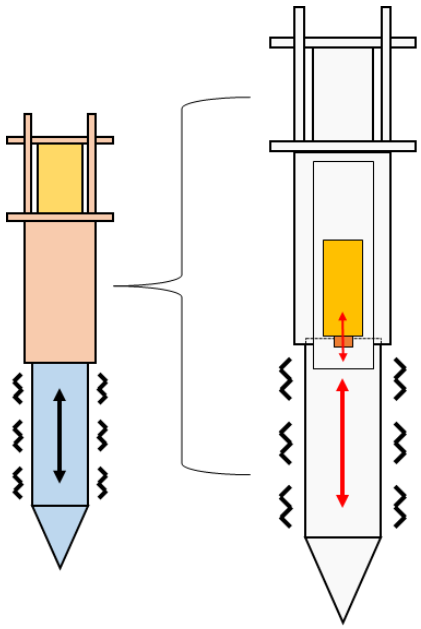

Figure 4.4: Diagram of how to achieve percussion using a piezoelectric stack actuator.

Regarding the failure of the spring pin for the follower link, if a slider crank mechanism is chosen to be used for future study of the prototype, the resilience of the pin-follower link interface will have to be increased. This could potentially be done by adding spacers on the pin to keep the follower link centered along its length and to prevent it from moving toward one end or the other which would place unwanted forces on the system. It would also be potentially helpful to replace the spring pin with a dowel pin, which is solid and more uniform, and therefore more resilient to stress concentrations than a spring pin.

4.3 Root Casing Subsystem Conclusions and Recommendations

According to the penetration depth tests, the anchoring system was able to penetrate at least 9 inches (0.2286 m) into the regolith simulant at a velocity of 3 m/s. The original goal defined in the critical design report was for the anchor to penetrate 10 inches at 5 m/s and the system was able to reach that goal at 3 m/s. It behaved exceptionally well and its design helped prove the usefulness of the closed form solution as demonstrated in Section 4.5.1.

The cone tip showed no damage after repeated impact with the regolith. The cone shape could be improved by increasing the angle on it so it pierces through the regolith better and decreasing the thickness of the walls. The added wall thickness increased the weight of the device and it was over designed for the soft regolith environment.

The casing tube could be improved by adjusting the angle on the root holes. The roots had a difficult time extruding from the root casing so adjusting the angle and size of hole could help improve its performance. The original design was for eight roots to deploy 0.2 m from the casing but the casing only allowed for four roots to deploy 0.0254 m from the casing. This reduction in root surface area caused them to be ineffective during the pullout force tests. The casing tube could be improved by reducing the diameter of the tube. The diameter of the tube has an inverse impact on the penetration depth of the

anchoring system and having a smaller diameter greatly increases the penetration depth. Reducing the diameter would require a denser configuration for the root system.

The performance of the compliant flaps overshadowed the root system drastically. Once the penetration depth reached 0.2286 m, the compliant flaps had enough area to engage with the regolith simulant and showed ideal pullout characteristics by anchoring onto the regolith walls. The compliant flaps could be improved by moving them closer to the anchor cone tip in order for them to be engaged at lower penetration depths. The material thickness of the flaps could be adjusted in order to create a comparison between the performance of stiff and flexible compliant flaps.

4.4 Damper Conclusions and Recommendations

Based on the compression tests of the honeycomb damping material and the calculation of impact force on the damper, it was predicted that the damper material would totally crush, absorbing a portion of the impact energy. After testing it was observed that the damper material was crushed, as predicted. The test data shown in Table 3.4 shows that the damper led to an average of about 24% reduction in acceleration between the anchor and lander side of the damper. This means that the damper was effective in absorbing some of the excess impact energy.

Moving forward there is additional testing that should be done for the damper. First, based on compression tests, it was clear that the Nomex Hexcel honeycomb material had a crush strength significantly lower than the max value that would prevent it from crushing. The Nomex honeycomb was chosen due to its availability, and if there was room in the budget for more damping material other versions of the honeycomb with higher compressive strength would have been tested. An analysis using the accelerometers would be used to investigate how the change in damping material properties affected the performance of the damper. Securely fastening the accelerometers to the damper plates will also be important to reduce noise from vibrations.

Lastly, many more iterations of each test would ideally be completed to provide more accurate conclusions about the subsystem. Budget constraints limited the amount of damping material available as well as regolith simulant foam. This led to the number of tests performed to be less than ideal.

4.5 Correlating Results to Models

One main focus of testing is to ensure that the Talus Low-G Anchoring System behaves similar to the design requirements based on the closed form solutions developed for penetration depth and anchoring force. If these components correlate well, then predictive models can be developed to calculate future performances based on variations to the original design and for different celestial surface properties.

4.5.1 Penetration Depth

As mentioned above, one of the primary goals of testing is to compare experimental penetration results with the closed form solution, shown below in equation (4.1), in order to create a predictive model for varying parameters such as regolith compressive strength, diameter of anchor, velocity, and anchor tip shape. More detail about the penetration depth calculations can be found in section 7.3 Appendix C.

$$X = \frac{2M}{\pi d^2 B\rho N_2} ln(1 + \frac{B\rho N_2 V_2}{AYN_1}) \qquad (4.1)$$

Figure 4.5 compares the closed form solution with the experimental results for both theoretical and measured velocities of the cone tip before impact. The closed form solution is based on the equations developed by Chen and Li [9] and it correlates well with experimental results especially when the frictional losses in the velocity are accounted for by directly measuring the bin speed using a camera and measurement board marked in 10 cm increments with 1 cm tick marks.

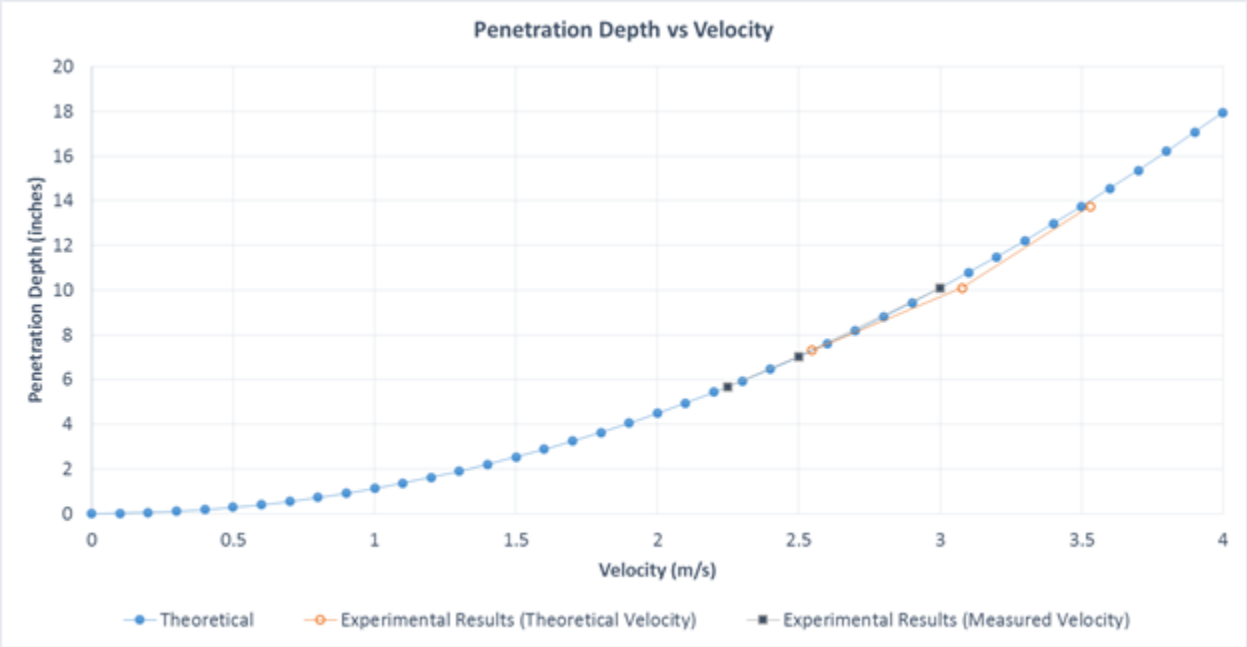

Figure 4.5: Penetration Depth Vs Velocity

Table 4.1 shows the penetration depths for the closed form solution and the theoretical velocity using energy balance and the % error ranged from 20%-30%. When accounting for the velocity losses in Table 4.2, that % error decreases to 3%-5% which demonstrates that the closed form solution correlates well with test results and can be used to predict future performances in varying environments.

Table 4.1: Penetration Depth Results (Theoretical Velocity)

Penetration Depth Results (Theoretical Velocity)				
Height (in)	Theoretical Velocity (m/s)	Theoretical Penetration (in)	Actual Penetration (in)	% Error
25	3.53	13.75	9.5	30.9%
19	3.08	10.1	7.25	28.2%
13	2.55	7.3	5.875	19.5%

Table 4.2: Penetration Depth Results (Measured Velocity Accounting for Frictional Losses)

Penetration Depth Results (Measured Velocity Accounting for Losses)				
Height (in)	Measured Velocity (m/s)	Theoretical Penetration (in)	Actual Penetration (in)	% Error
25	3	10.1	9.5	5.94%
19	2.5	7.02	7.25	3.28%
13	2.25	5.68	5.875	3.43%

4.5.2 Pullout force

The closed form solution for determining the extraction force required to remove an anchor from regolith is based on the work done by Biele, Ulmacec, Knollenber, Kuhrt, and Mohlmann. The article describes determining the extraction force as "a more difficult issue to estimate" and describes lower and upper limits for estimating the extraction force [8]. The lower and upper limits are described below in equations 4.2 and 4.3.

$$F_{min} = A_h \sigma_c \quad (4.2)$$
$$F_{max} = S_h d \sigma_c \quad (4.3)$$

In the lower limit force equation, A_h represents the surface area of the anchoring system under the regolith. For the Talus anchoring system, this area would represent the top down area of the extended root system and the compliant flaps over the root casing tube. The variable σ_c represents the compressive strength of the regolith which can vary between 7 kPa and 100 kPa on comet 67P [8]. As a reference, snow varies between 5.9-86 kPa depending on the compactness of snow [8]. The regolith simulant tested has a compressive strength of 62.5 kPa which is in range of comet 67P estimates.

Using the area, perimeter values measured from the prototype, and the regolith simulant compressive strength of 62.5 kPa, the minimum and maximum anchoring forces are 99.8 N and 3975 N respectively. More details about the calculations can be found in 7.3.1 Appendix C. The theoretical extraction force values have a large range. When designing a system for unknown conditions, it is important to use the minimum value to ensure that the anchor is designed for the least favorable parameters because this ensures that it will work for the upper limit force parameters.

In order to validate the range of values given in the closed solution, pullout force calculations were measured for the prototype within the regolith simulant. The prototype was designed to penetrate the regolith at a depth of 9 inches (0.23 m) with an impact velocity of 3 m/s. Once the system impacted the regolith as seen in Figure 4.6, the roots were deployed and the system was slowly pulled out of the regolith bin with a force gage. Multiple tests were conducted in order to get a large sample size and the average pullout force was 35 lbf, with the roots deployed, which equates to 154 N. The 154 N pullout force falls within the range defined by the theoretical pull out force equations and it resides closer to the lower limit of 99.8 N. This demonstrates that the pullout force is more dependent on the projected surface area of the deployed roots and the compliant flaps than the perimeter and depth. Further improvements to the design of the anchoring system will be in accordance to the pullout force lower limit.

Figure 4.6: Device penetrating regolith past compliant flaps

Figure 4.7: Extraction test with roots fully extended

4.6 Sources of Error

There are a few sources error that could have occurred during the two tests. For both tests, there is some level of inconsistency from the test rig itself. During the test, due to limitations of the location the test rig was used, the test rig was not constrained to the ground which allowed it to move freely while in use. This may have altered the perceived effectiveness of the anchoring system. To mitigate this issue, two weights were placed at the base of the test rig. Even with precautionary measures in place, a small bit of error from displacement should be noted.

The impact between the anchoring system and the regolith was not perfectly perpendicular. If the impact is not perpendicular then energy is being wasted, consequently shortening the penetration depth. Once the pendulum arm locked into place at full vertical, the entire rail that the regolith bin slides on continued to rotate upwards. This essentially caused the regolith bin to move upwards. This upwards motion caused the anchoring system to impact the regolith at an angle. The result of this angled impact can be seen in the regolith after the anchoring system is pulled out during the pull out test. In Figure 4.8 below it can be seen that the hole in the regolith is larger than the anchoring system. This can be partly due to the flaps on the root casing; however, the hole is more oval shaped. The oval shaped hole at the surface of the regolith is not centered with the rest of the interior of the hole. This means the anchor must have hit the regolith at an angle. The best way to mitigate this for future experiments would be to increase the distance that the regolith bin slides before impacting the anchoring system.

Figure 4.8: Angled impact between anchoring system and regolith

During the pullout test, a spring gauge was used. During the manual pullout test, the anchoring system and regolith were pulled apart slowly. This was done so that the force reading would be strictly reading the pullout force and not the force to accelerate the regolith bin. Although done slowly, possible inconsistencies in movement could have resulted in error with the measurement device that would lead to an overestimate of the pullout force. For future testing, a measurement device that pulls with a consistent motion would be desired. .

The regolith simulant was composed of multiple blocks of foam. In order to efficiently use the limited supply of foam, only the foam blocks that were damaged during the previous test were replaced. Some of the blocks in the back that were not visibly damaged may have suffered slight compression, thus slightly altering results of future tests that used the same blocks. The severity of this issue is likely very miniscule. Even though the blocks were packed tightly together, there could have been some movement

between each block during impact. Ideally, one large continuous block would be used for testing and would be replaced after each test.

The onboard accelerometers were mounted directly to the test rig and as a result, vibrations from the percussive digging mechanism created a substantial amount of noise in the output graphs. This made the desired measurements difficult to obtain. Figure 4.9 displays the acceleration data obtained from Test 11; a test that included the percussive digging mechanism. The plot is scaled such that 100 samples are collected per second.

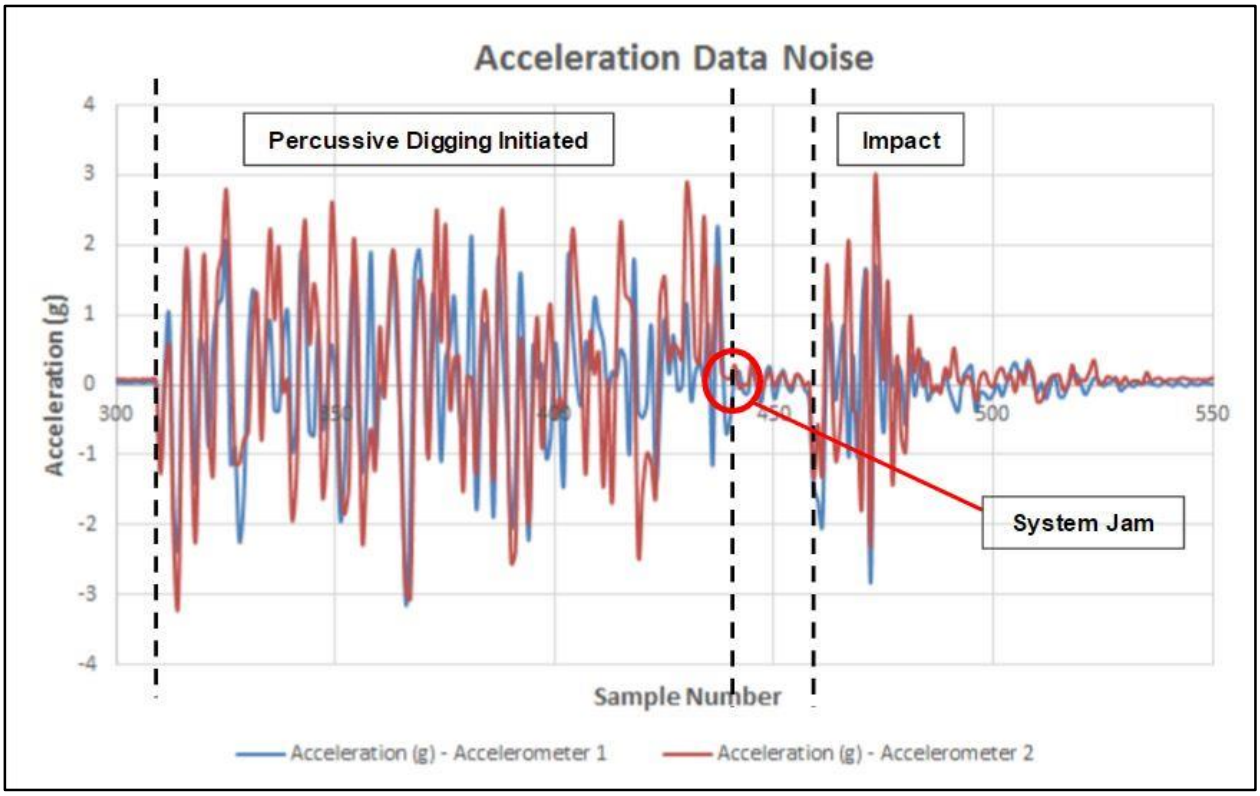

Figure 4.9: Acceleration data noise for Test 11

It is evident that after the percussive digging mechanism is initiated just after sample 300, it interferes with and invalidates any decipherable acceleration reading until around sample 450; when the percussive system jammed just as the regolith box was released. This short amount of time provides a reference for the previously obtained data. The percussive digging mechanism, operating at about 15 Hz with half power, induces an external system noise with an amplitude of about plus or minus 3g. This matches scale almost identically to the response created from regolith impact. With this information it is difficult to trust any accelerometer data obtained from the tests featuring percussive damping. Future tests would require some sort of damping technique to isolate the accelerometers from the shaking caused by the percussive digging system when in use.

4.7 Future Testing

For the current prototype, insufficient testing was performed on the Percussive Digging Subsystem due to technical complications. Therefore it is recommended that further testing be performed with the percussive motion of the prototype enabled during impact in order to properly characterize the subsystem's performance.

In addition, the Root Subsystem would benefit from further testing since observations during the initial testing indicated that the compliant flaps overshadowed any effect of the roots at providing an anchoring force. Future tests should involve the removal of the flaps and measurement of the pullout force with the roots engaged in order to determine their effectiveness.

The damping subsystem's performance could be validated further by obtaining accelerometer data from an impact case without any damping material loaded into the prototype. This would illustrate a worst case scenario of what the impact would look like with no damping system or for a critical damping system failure.

In addition to the above, the validation of the prototype as a whole would benefit from additional trials for every test performed. Time constraints during the initial round of testing allowed for only 3 trials per experiment. Additional trials would serve to more accurately portray the performance of the prototype.

5.0 Conclusion and Marketing of the Final Product

Development and testing of the Talus Low-G Anchoring System thus far has shown it to be more effective than the benchmark lander in several key ways such as a reduced complexity and greater effective anchoring force. The prototype differs from the benchmark in that it is heavier and larger, although with further development of the concept, the size will be brought down through employing the use of composite materials and tighter packaging of mechanical components. The competitive performance shown in testing is promising for the maturation and development of this concept toward a final product.

Considerations for the future of this program come with implications of publicizing the success of the product to the industry. Given the new and upcoming desire by government and private entities to send spacecraft to small astronomical bodies, a promising anchoring device like the Talus Low-G Anchoring System will soon be in high demand. With further development of the current prototype, the concept can be publicized at industry conferences and published in technical journals as the state of the art solution for spacecraft intended to work in a low-g environment. With public knowledge of the system's potential, it will soon be incorporated into the spacecraft design of missions to low-g astronomical bodies.

6.0 Citations

[1] European Space Agency, "THREE TOUCHDOWNS FOR ROSETTA'S LANDER," 14 November 2014. [Online]. Available: http://m.esa.int/Our_Activities/Space_Science/Rosetta/Three_touchdowns_for_Rosetta_s_lander. [Accessed January 2016].

[2] Planetary Resources, "Planetary Resources: Asteroids," Planetary Resources, 22 January 2016. [Online]. Available: http://www.planetaryresources.com/asteroids/#mining-delivery. [Accessed 30 January 2016].

[3] Deep Space Industries, "Space Resources," Deep Space Industries Inc., [Online]. Available: https://deepspaceindustries.com/. [Accessed 29 January 2016].

[4] W. F. Rogers, "Apollo Experience Report," National Aeronautics and Space Administration, Houston, Texas, 1972.

[5] H. Liu, Z. Zhao and J. Zhao, "Preliminary Anchoring Technology for Landing on the Asteroid," *International Conference on Robotics and Biomimetics (ROBIO)*, Shenzhen, China, 2013.

[6] J. W. P. C. K. Z. K. D. J. Craft, "Percussive Digging Systems for Robotic Exploration and Excavation of Planetary and Lunar Regolith," in Aerospace Conference, 2009 IEEE, 2009.

[7] H. B. Mohammed M. Ettourney, "Regolith Mechanics, Dynamics, and Foundations," Journal of Aerospace Engineering, vol. 5, no. 2, 1992.

[8] J. Biele, S. Ulamec, L. Richter, J. Knollenberg, E. Kuhrt and D. Mohlmann, "The putative mechanical strength of comet surface material applied to landing on a comet," *Acta Astronautica*, vol. 65, pp. 1168-1178, 2009.

[9] X. Chen and Q. Li, "Deep penetration of a non-deformable projectile with different geometrical characteristics," International Journal of Impact Engineering, vol. 27, pp. 619-637, 2002.

[10] F. Cain, "Universe Today," Universe Today, 2 July 2013. [Online]. Available:http://www.universetoday.com/77070/how-cold- is-space/. [Accessed 1 January 2016].

7.0 Appendices

7.1 Appendix A: Swing Test Procedure

Table 7.1: Materials for Swing Test

Test	Swing Test
Relevant Documents	SR3
Materials:	**Notes:**
Talus Low-G Anchoring System prototype	
Test rig	
Regolith simulant	
Dry-erase marker	
Ruler or similar measurement device	
Laptop	
Extension cord	For laptop as needed
Extended Wires	For power to motors on device

Swing Test Procedure

1. Prepare test rig and prototype for the Swing Test. The prototype should be wired to the myRIO controller and the test rig should be packed with the simulant material at this time.
2. Integrate the test rig and prototype for the Swing Test. The prototype should be connected to its power source and ready to be activated.
3. Double check all systems and ensure all safety requirements as specified in the SR3 memo are met.
4. Set the prototype's height by pulling the rope until the box's marked datum is 42" above the ground.
5. Initiate the test by first activating the accelerometer data collection, and then the percussive digging system (if required by the experiment). Immediately release the pendulum arm from its raised position.
6. After impact with the test medium, ensure that the prototype has come to rest and is shut down.
7. Mark the depth that the prototype has penetrated into the test medium by using the dry-erase marker to mark the top of the prototype shell (the Casing Tube).
8. Proceed to Pullout Test procedure.

7.2 Appendix B: Pullout Test Procedure

Table 7.2: Materials for Pullout Test

Test	Pullout Test
Relevant Documents	SR3
Materials:	**Notes:**
Talus Low-G Anchoring System prototype	
Test rig	
Regolith simulant	
Spring scale or similar force transducer	
Laptop	
Extension cord	For Laptop as needed
Extended Wires	For power to motors on device

Pullout Test Procedure

1. Continue starting from the end of the Swing Test. The prototype should be embedded in test medium and untouched from the end of the Swing Test procedure. The prototype should be connected to its power source and ready to be activated.
2. Double check all systems and ensure all safety requirements as specified in the SR3 memo are met.
3. Secure the spring scale to the back of the regolith box.
4. If required for the experiment currently being conducted, fully activate the root system. Ensure the root system has deployed, then shut down the prototype.
5. Configure test rig so that the prototype can be pulled out of the test medium.
6. Begin slowly and steadily pulling the prototype out of the test medium until the prototype disengages from the test medium.
7. Record the peak force as measured by the spring scale. This is the Pullout force of the anchor system.
8. Reiterate the experiment by returning to the Swing Test procedure. Repeat the whole process as many times as necessary to obtain useful results.

7.3 Appendix C: Analytical Calculations and Results

7.3.1 Appendix C: Soil/Regolith Penetration Calculations

Table 7.3: Penetration Depth Nomenclature

Nomenclature			
Variable	Description	Value Range	Units
P	Soil porosity	0.8	-
V	Velocity of anchoring tip	1 - 5	m/s
Θ	Angle of cone tip	30	Degrees
Y	Yield stress	7,000 - 100,000	N/m^2
ρ	Soil density	200 - 500	kg/m^3
ρ_c	Soil initial density	-	kg/m^3
ρ*	Soil locked density	-	kg/m^3
M	Mass of anchor and lander per leg	25	kg
h	Height of cone	0.0550	m
d	Diameter of anchor	0.0635	m
N1	Friction factor	1	-
N2	Shape factor	0.25	-
F_x	Axial resistive force	-	N
A	Soil material constant	1.74	-
B	Soil material constant	1.07	-
X	Penetration depth	-	m
I*	Dimensionless impact factor	-	-
$\boldsymbol{\lambda}$	Dimensionless mass ratio	-	-
N	Geometric function of projectile	-	-
I	Impact function	-	-
n*	Locking volumetric strain	-	-
μ_m	Sliding friction	0	-
σ_t	Tangential stress	0	N/m^2
σ_n	Normal Compressive Strength	-	N/m^2

Assumptions

Neglect sliding friction from cone tip to soil → N1 = 1
Cone tip is rigid and has no deformation
Neglect gravity
Neglect crater depth

Resistive Force Calculation for Cone and Casing [9]

$$F_x = \frac{\pi d^2}{4}(AYN_1 + B\rho V^2 N_2)$$

$$N_1 = 1\ (assume\ sliding\ friction = 0)$$

$$N_2 = sin^2\,\theta = sin^2\,(30)\ \ = 0.25\ (cone\ shape\ factor)$$

$$n^* = 1 - \frac{\rho_c}{\rho^*} = 1 - 0.8 = 0.2$$

$$A = \frac{2}{3}(1 - ln\,(n^*)\,) = 1.74$$

$$B = (n^*)^{1/3} + [\frac{3 - (n^*)^{\frac{1}{3}}(4 - n^*)}{2(1 - n^*)}] = 1.07$$

$$F_x = \frac{\pi(0.0635\,m)^2}{4}((1.74)Y(1) + (1.07)\rho V^2(0.25))$$

Resistive force is a function of compressive strength, density of the soil and the velocity of the anchor making impact with the soil. Soil conditions will be unknown during a landing so each condition should be considered.

Table 7.4: Resistive force calculations

Resistive force calculations with varying parameters			
Y (N/m^2)	ρ (kg/m^3)	V (m/s)	F_x (N)
7,000	200	1	38.7
7,000	200	5	42.8
7,000	500	1	39.0
7,000	500	5	49.2
100,000	200	1	551.1
100,000	200	5	555.2
100,000	500	1	551.3
100,000	500	5	561.5

From the table above, the compressive strength of the soil has the largest impact on the force resistive force of the soil.

Penetration Depth Calculations for Cone and Casing

From derivations with the resistive force equation [9]

$$F_x = \frac{\pi d^2}{4}(AYN_1 + B\rho V^2 N_2)$$

$$X = \frac{2M}{\pi d^2 B\rho N_2} ln\,(1 + \frac{B\rho N_2 V^2}{AYN_1})$$

$$I^* = \frac{MV^2}{d^3 Y}$$

$$\lambda = \frac{M}{\rho d^3}$$

$$N = \frac{\lambda}{BN_2}$$

$$I = \frac{I^*}{AN_1} = \frac{I^*}{A}$$

$$\frac{X}{d} = \frac{2}{\pi} N ln(1 + \frac{I}{N})$$

$$X = \frac{2}{\pi} N ln(1 + \frac{I}{N}) d$$

Table 7.5: Penetration depth with varying parameters

Penetration depth calculations with varying parameters				
Y (N/m^2)	ρ (kg/m^3)	V (m/s)	X (cm)	X (in)
7,000	200	1	25.5	10.0
7,000	200	5	636.4	250.6
7,000	500	1	25.5	10.0
7,000	500	5	636.4	250.6
100,000	200	1	1.8	0.7
100,000	200	5	44.5	17.5
100,000	500	1	1.8	0.7
100,000	500	5	44.5	17.5

Density of the material has a small impact when dealing with penetration force for a soil with a relatively small velocity of 1 and 5 m/s. Compressive strength of the soil and the anchoring velocity have the largest impact on penetration depth. As the compressive strength increases, more velocity is needed to obtain an ideal penetration depth of 0.254 m. The Philae lander made impact with comet 67P which caused 0.1 to 0.2 m of penetration so it has been assumed that the top layer is around 10 inches thick and has a small compressive strength and then the material underneath becomes harder. If the soil penetration is deeper than expected, then the lander legs will help to reduce the penetration by increasing the area making contact with the surface.

Anchoring Force for Compliant Flaps

For the regolith flaps, it is assumed that the depth is ideal so the flaps will have 3 in of soil above it during deployment. The area of the flaps is 2.06 in^2 and the compressive strength varies between 7 and 100 kPa. The minimum force required to pull out an object is a function of the compressive strength of the soil and the area of the flaps based on documentation from reference [8].

$F_{min} = \sigma_c A = YA$

From this equation, the force of the regolith will be 9.28 N up to 132 N if the compressive strength varies from 7 kPa to 100 kPa respectively.

7.3.2 Appendix C: Pullout Force Closed Form Solution for wet dry foam properties

Table 7.6: Pullout force nomenclature

Nomenclature			
Variable	Description	Value Range	Units
L_r	Length of root	0.0254	m
L_f	Length of compliant flap	0.0348	m
A_h	Surface area of root and flaps	0.001597	m^2
σ_c	Compressive strength of regolith	62,500	N/m^2
S_h	Perimeter of roots and flaps	0.310	m
d	Depth from surface to cone tip	0.2413	m
n_r	Number of roots	4	-
d_{r1}	Depth of root 1 above the surface	0.1651	m
d_{r2}	Depth of root 2 above the surface	0.1524	m
d_{r3}	Depth of root 3 above the surface	0.1397	m
d_{r4}	Depth of root 4 above the surface	0.1270	m
n_f	Number of compliant flaps	6	-
d_f	Depth of flaps above surface	0.0203	m
F_{min}	Minimum pullout force	-	N
F_{max}	Maximum pullout force	-	N

Upper and lower anchor forces are described below in equations 1 and 2 from reference [8].

$$F_{min} = A_h \sigma_c \quad (1)$$

$$F_{max} = S_h d \sigma_c \quad (2)$$

Area is broken down into the normal projected area of the roots and flaps when looking top down onto the deployed anchoring system.

$$F_{min} = (0.001597\ m^2)(62{,}500\ N/m^2) = 99.8\ N$$

Perimeter and depth can be broken down for each individual root because each root is at a different height within the regolith. Roots are staggered. Assuming a penetration depth of 0.2413 m (9.5 inches) which was the measured penetration depth after testing at a velocity of 3 m/s.

$$F_{max} = \{[L_r(d_{r1} + d_{r2} + d_{r3} + d_{r4})] + (L_f * d_f)\}\sigma_c$$

$$F_{max} = \{[0.254\ m(0.1651\ m + 0.1524\ m + 0.1397\ m + 0.1270\ m)] + (0.0348\ m * 0.0203\ m)\}62{,}500\ N/m^2$$

$$F_{max} = 3975\ N$$

Range of anchoring force is between 99.8 and 3975 N for a compressive strength of 62,500 N/m^2. Experimental pullout force averaged 154 N which is closer to the minimum pullout force calculation which means F_{min} should be used for predicting pullout forces for anchoring systems with varying root and compliant flap properties.

7.3.3 Appendix C: Percussive Digging Subsystem

Slider-Crank Kinematic Analysis

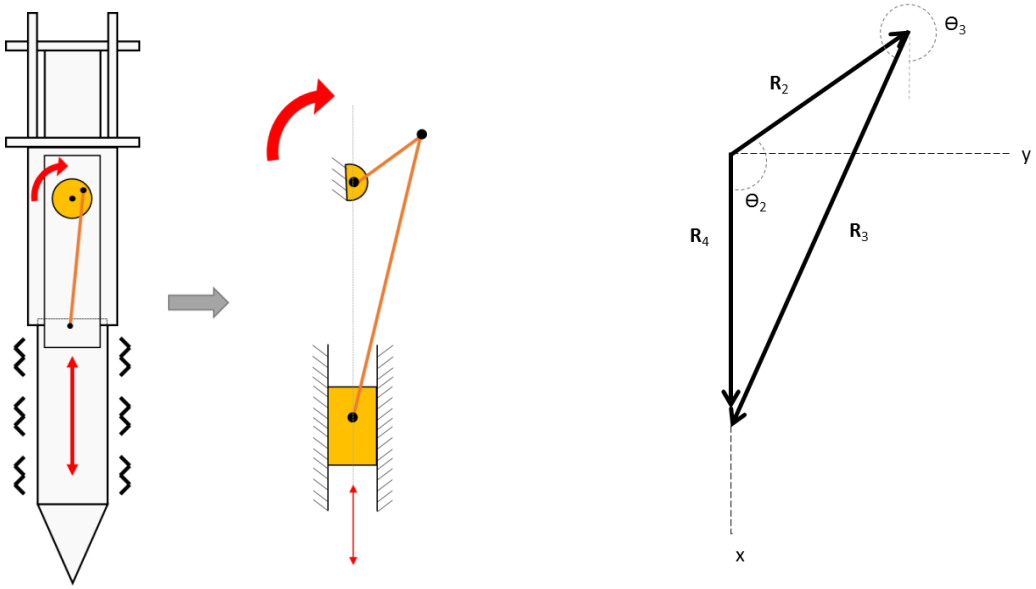

Vector Loop:

$\vec{R_2} + \vec{R_3} - \vec{R_4} = 0$

Angles & lengths:

$\theta_4 = 180°$

$\theta_3 = tan^{-1}\left[\frac{R_2 sin(\theta_2)}{R_4 - R_2 cos(\theta_2)}\right]$

$R_4 = R_2 cos(\theta_2) + \sqrt{R_3^2 - (R_2 sin(\theta_2))^2}$

X components:

$$X: \quad R_2 cos(\theta_2) + R_3 cos(\theta_3) - R_4 cos(\theta_4) = 0$$

$$X': \quad -R_2 sin(\theta_2) - R_3 sin(\theta_3)\,\theta_3' - R_4' cos(\theta_4) = 0$$

$$X'': \quad -R_2 cos(\theta_2) - R_3 cos(\theta_3)\,\theta_3'^2 - R_3 sin(\theta_3)\,\theta_3'' + R_4' sin(\theta_4) - R_4'' cos(\theta_4) = 0$$

Y components:

$$Y: \quad R_2 sin(\theta_2) + R_3 sin(\theta_3) - R_4 sin(\theta_4) = 0$$

$$Y': \quad R_2 cos(\theta_2) + R_3 cos(\theta_3)\,\theta_3' - R_4' sin(\theta_4) = 0$$

$$Y'': \quad -R_2 sin(\theta_2) - R_3 sin(\theta_3)\,\theta_3'^2 + R_3 cos(\theta_3)\,\theta_3'' - R_4' cos(\theta_4) - R_4'' sin(\theta_4) = 0$$

Kinematic coefficients:

$\theta_3' = -\frac{R_2 cos(\theta_2)}{R_3 cos(\theta_3)}$

$\theta_3'' = \frac{R_2 sin(\theta_2)}{R_3 cos(\theta_3)} + tan(\theta_3)\,\theta_3'^2$

$R_4' = -R_2 sin(\theta_2) + R_2 cos(\theta_2)\,tan(\theta_3)$

$R_4'' = -R_3 sin(\theta_3)\,\theta_3'' - R_2 cos(\theta_2) - R_3 cos(\theta_3)\,\theta_3'^2$

Velocity & acceleration:

$\dot{R}_4 = R'_4\dot{\theta}_2$

$\ddot{R}_4 = R''_4\dot{\theta}_2^2 + R'_4\ddot{\theta}_2$

$\ddot{\theta}_2 = 0$

Impact Energy:

Impact energy is equivalent to E, the kinetic energy of the barb assembly. m_b is the mass of the barb assembly and the speed of the assembly is $\dot{R}_4$. The required rotational speed output by the driving motor is determined from the desired impact energy. $R'_{4,max}$ is the value of the kinematic coefficient corresponding to when the barb is traveling the fastest.

$$E = \frac{1}{2}m_b(\dot{R}_4)^2 = \frac{1}{2}m_b(R'_4\dot{\theta}_2)^2$$

$$\dot{\theta}_2 = \frac{1}{R'_{4,max}}\sqrt{\frac{2E}{m_b}}$$

Force Analysis

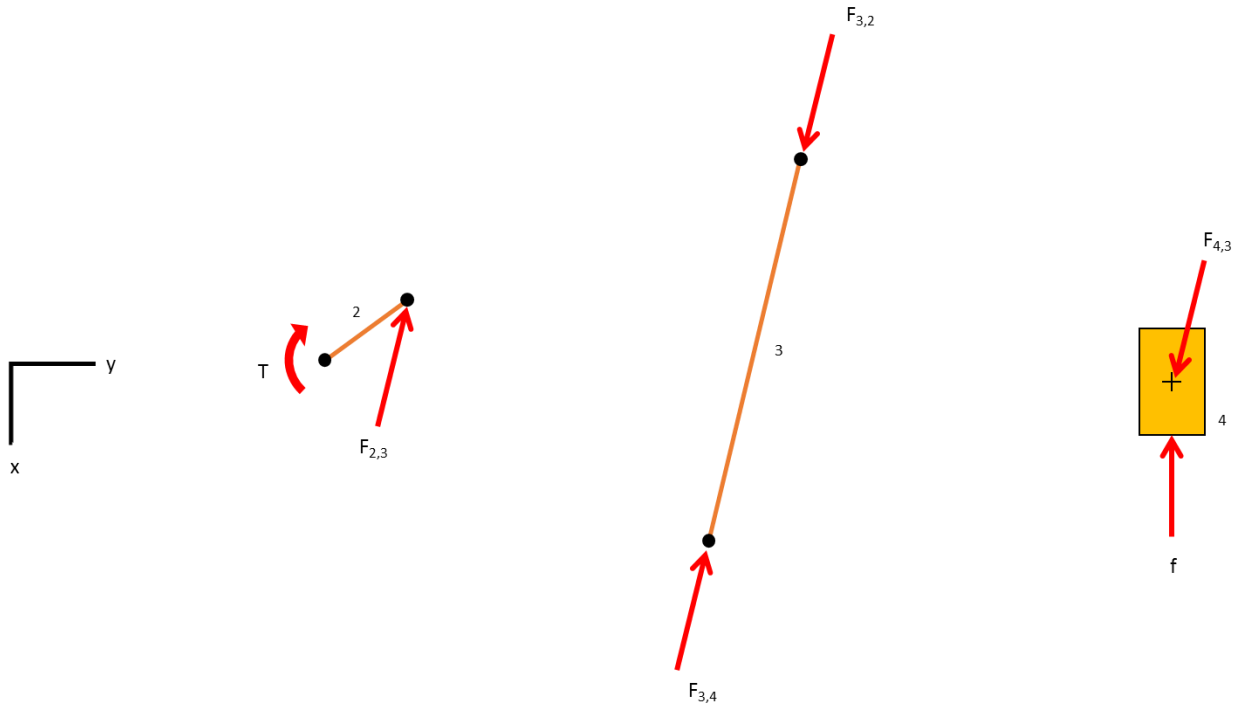

Assumptions:

- Links 2 and 3 have negligible mass
- friction from regolith negligible when compared to inertial forces
- Gravitational forces negligible

$$\sum F_{4,x}: \quad m_b \ddot{R}_4 = F_{4,3} cos\,(\theta_3) - f$$

$$\sum F_{3,x}: \quad 0 = F_{3,2} cos\,(\theta_3) - F_{3,4} cos\,(\theta_3)$$

$f \cong 0$

$F_{3,2} = F_{3,4} = -F_{4,3} = -F_{2,3}$

$$\sum M_{origin}: \quad 0 = -T + F_{2,3} cos\,(\theta_3)\ R_2$$

$$T = F_{4,3} cos\,(\theta_3)\, R_2 = F_{4,3} R_2 [\frac{R_4 - R_2 cos\,(\theta_2)}{R_3}]$$

$$F_{4,3} = \frac{f + m_b \ddot{R}_4}{cos(\theta_3)} = \frac{f + m_b \ddot{R}_4}{[\frac{R_4 - R_2 cos\,(\theta_2)}{R_3}]}$$

$T = R_2 [f + m_b \ddot{R}_4]$

Electrical design:

Vaa = 24 V
Q1: IRF520
D1: 1N4001
RY1: LEV200H5ANA

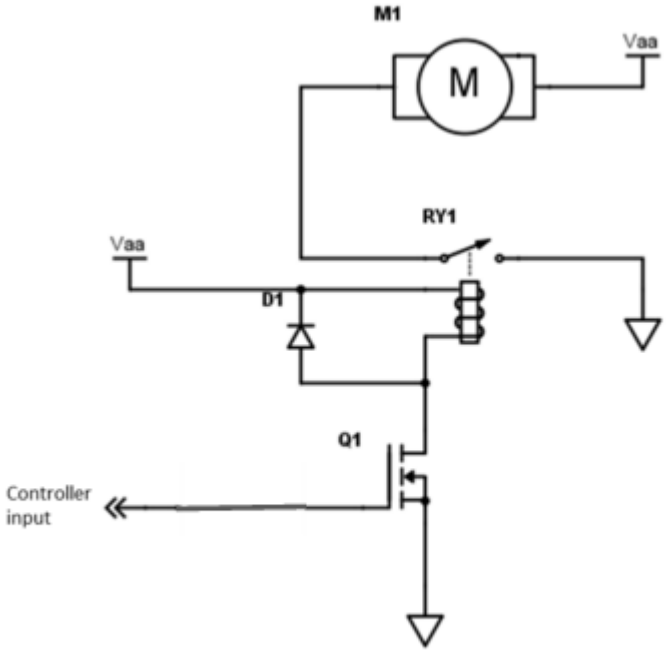

7.3.4 Appendix C: Root Calculations

Root Length

Inputs:

$D_c = Inner\ Diameter\ of\ casing = 2"$

$D_R = Diameter\ of\ root = \frac{1}{4}"$

$N = Number\ of\ turns = 3$

$D_0 = Radius\ of\ first\ loop = \frac{1}{2}"$

Calculations:

$L_R = Length\ of\ root = \pi N(D_o + D_R(N-1)) = 3\pi(\frac{1}{2} + \frac{1}{4}(3-1)) = 9.4$

"Roll length calculator," *Roll length calculator*. [Online]. Available at: http://www.giangrandi.ch/soft/spiral/spiral.shtml. [Accessed: 06-Mar-2016].

Root Anchoring Force

Inputs:

$N_R = Number\ of\ roots = 8$

$D_f = Diameter\ of\ frayed\ tip = 1"$

$S_u = Asteroid\ Strength = 1.02\ psi$

Calculations:

$A_f = Anchoring\ Area\ of\ frayed\ tip = \frac{1}{4}\pi(D_f^2 - D_R^2) = .147\ in^2$

$P_f = Perimeter\ of\ frayed\ tip = \pi D_f = 1.57\ in$

$F_{R1} = Root\ Anchoring\ Force\ Estimate\ 1 = A_f S_u = .15\ lbs$

$F_{R2} = Root\ Anchoring\ Force\ Estimate\ 2 = P_f L_R S_u = 15.95\ lbs$

$F_{A1} = Anchoring\ Force\ Estimate\ 1 = NF_{R1} = 1.20\ lbs$

$F_{A2} = Anchoring\ Force\ Estimate\ 2 = NF_{R2} = 127.6\ lbs$

Root Motor Torque

Inputs:

$A_{RT} = Area\ of\ root\ tip = \frac{1}{4}\pi D_f^2 = .196\ in^2$

$F_T = Root\ Thrusting\ Force = A_{RT} S_u = .20 lbs$

$T_R = Root\ Shaft\ Torque = \frac{D_c}{2} F_T = .199\ lbin$

$T_M = Motor\ Torque\ required = T_R N = 1.59\ lbin = .18 Nm$

Motor Driver Circuit

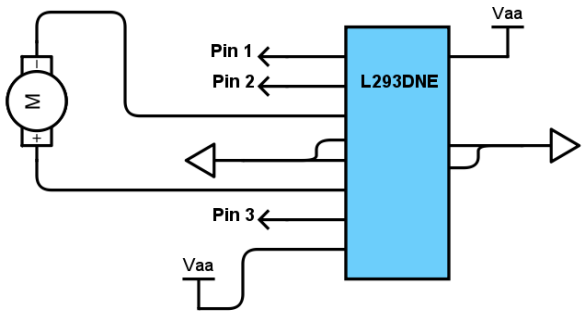

Root actuator motor driver circuit

7.3.5 Appendix C: Damping material Compressive Strength Limit

Variables

$m = lander\ mass = 25\ kg$
$V = impact\ velocity = 3\ m/s$
$A = area\ of\ damping\ material = 4\ in^2 = .0026\ m^2$
$d = estimated\ penetration\ depth = 0.1\ m$

The following is a calculation of the force seen the damping material during impact considering the penetration depth, lander mass, and impact velocity.

$Impact\ Force = 0.5mV^2/d = 0.5 * 25 * 3^2/0.1 = 1125\ N$

The maximum compressive strength for the damping material was calculated with the following equation considering the impact force and area of damping material. If the damping material has a higher compressive strength than the calculated value, the material will not crush or absorb excess energy.

$Newtons\ per\ square\ inch\ of\ honeycomb = impact\ force/A = 1125/.0026 = 430\ MPa$

This calculation shows that if the honeycomb has a compressive strength over 430 MPa the damper will not compress. The honeycomb available to team talus for testing had a compressive strength of approximately 208.4 kPa (test data shown in Appendix D), therefore was significantly less than the maximum value.

7.4 Appendix D: Compressive Strength Testing Results

Table 7.7: Phenolic foam compressive strength trials

Trial	Force to Crush [N]	Crush Area [m^2]	Compressive Strength [N/m^2]
1	34.8	5.573E-04	62413
2	38.4	6.334E-04	60610
3	42.8	6.984E-04	61274
4	41.2	6.824E-04	60424
5	40.7	6.965E-04	58502
6	45.9	6.478E-04	70860
7	47.3	7.319E-04	64609
8	40.4	6.645E-04	60781
9	39.3	5.794E-04	67873
10	37.0	6.387E-04	57874
			Avg. = 62521 N/m^2

Table 7.8: Nomex Hexcel Honeycomb Compressive Strength Trials

Trial	Force to Crush (N)	Area (m^2)	Compressive Strength [N/m^2]
1	177.484	9.68E-04	183351.24
2	217.963	9.68E-04	225168.39
3	197.946	9.68E-04	204508.26
4	213.515	9.68E-04	220573.35
			Avg = 208.4 kPa

7.5 Appendix E: Bill of Materials

Project Talus Bill of Materials			Total Cost	$360.85		
			Remaining Budget	$39.15		
Talus Part No.	Description	Manufacturer Information	Unit Price	Qty.	Total Cost *fill in this cell if part purchased through ME business office	
03_001	Motor mount plate	8975K446 (McMaster) 8"x6"	$31.74	1	$31.74	received
03_002	Motor mount bracket	8975K106 (McMaster) 6"x10"	$22.39	1	$22.39	received
03_003	Crank link	1610T15 (McMaster) 3"	$12.60	1	$12.60	received
03_004	Follower link	89015K275 (McMaster) 6"x6"	$11.74	1		
	18-8 Clevis Pin (D 3/16" , L 3/4")	92390A102(McMaster) x10	$7.91	1	$7.91	received
	18_8 Slotted Spring pin (D 3/16", L 2.5")	92373A267 (McMaster) x25	$11.61	1	$11.61	received
	Aluminum Spacer (D 1/4", L 1/8", 8 Screw Size)	92510A460(McMaster) x10	$0.23	10		
	Set screw 5-40(L 0.5")		$4.72	1		
	Steel clamp	3039T21(McMaster)	$4.13	2	$8.26	received
	Clamp bolt					
	Zinc-Plated Steel Cotter Pin (D 3/32", L 1/2")	98338A130 (McMaster)x100	$2.25	1		
	8-32 SHCS			1		
	Key stock (1/8"x1/8")	98830A100 (McMaster) 12"	$0.66	1	$0.66	received
03_M1	E30-400 Motor	Ampflow		1		
03_Relay1	LEV200H6ANA Relay	N/A		1		
03_D1	Rectifier/diode	78-VS-UFB250FA60 (Mouser)	$23.66	1	$23.66	received
03_R1	10k Resistor	N/A		1		
03_U1	MOSFET Transistor	942-IRLB3034PBF(Mouser)	$3.34	2	$6.68	received
	Perfboard	589-7100-45 (Mouser)	$4.99	1	$4.99	received
01_U1	H-Bridge SN754410	COM-00815 (Sparkfun)	$2.35	1	$2.35	received
01_001	Aluminum 6061 Solid Bar 3" OD, 3" height	8974K82 (McMaster) 3" OD, 1' length (check shop for s	$54.92	1	$54.92	received
01_002	Aluminum 6061 2.5" OD, 3/16" walls, 12" walls	http://www.ebay.com/itm/6061-T6-Aluminum-Roun	$17.50	1	$17.50	received
01_003	Same as above	Same as 01_002	$0.00	0		
05_001	Aluminum 6061 Solid Bar	Same as 01_001	$0.00	0		
05_002	Aluminum 6061 2.5" OD, 3/16" walls - tube	http://www.ebay.com/itm/6061-T6-Aluminum-Roun	$17.50	1	$17.50	received
05_003	Aluminum 6061 3" OD, 0.25" walls - tube	9056K21 (McMaster) 1' length	$36.37	1	$36.67	received
05_A1	3 Axis Accelerometer Breakout	ADXL335 (https://www.sparkfun.com/products/9269)	$14.95	2	$29.90	received
02_002	Aluminum Spacer (ID 1/2" , OD 2")	8975K418 (McMaster) 4"x 12"	$4.59	1		
02_003	Shaft (OD 1/2")	1031K13 (McMaster)	$10.03	1	$10.03	received
02_004	Bushing	6389K355 (McMaster)	$0.81	8	$6.48	received
02_005	Shaft Collar	9414T6(McMaster)	$1.00	8	$8.00	received
02_005	Shaft Collar	6432K17 (McMaster)	0.9	16	14.4	received
04_003	Rod	91025A570 (McMaster)	$1.82	4	$7.28	received
04_002	Top Plate	9246K11 (McMaster)	$14.80	2		
04_001	Bottom Plate	1610T17(McMaster)	$5.10	1		
02_003 Rev. 2	12" Aluminum Rod	8974K28 (McMaster)	$3.08	1	$3.08	received
04_003 Rev. 2	8" Rod	90575A223	$1.70	4	$6.80	received
	sparkfun order shipping				$8.20	
	sparkfun order2 shipping				$7.24	
Totals					$360.85	

7.6 Appendix F: Part Drawings